Earth and Space Science

RESEARCH ARTICLE
10.1029/2023EA003258

A Geostratigraphic Map of the Rachmaninoff Basin Area: Integrating Morphostratigraphic and Spectral Units on Mercury

Jack Wright[1,2], **Francesca Zambon**[3], **Cristian Carli**[3], **Francesca Altieri**[3], **Claudia M. Pöhler**[4], **David A. Rothery**[2], **Carolyn H. van der Bogert**[4], **Angelo Pio Rossi**[5], **Matteo Massironi**[6], **Matthew R. Balme**[2], **and Susan J. Conway**[7]

[1]European Space Agency (ESA), European Space Astronomy Centre (ESAC), Villanueva de la Cañada, Madrid, Spain, [2]School of Physical Sciences, The Open University, Milton Keynes, UK, [3]INAF-Istituto di Astrofisica e Planetologia Spaziali, Rome, Italy, [4]Institut für Planetologie, Universität Münster, Münster, Germany, [5]School of Science, Constructor University, Bremen, Germany, [6]Dipartimento di Geoscienze, Università degli Studi di Padova, Padova, Italy, [7]Laboratoire de Planétologie et Géosciences, CNRS UMR 6112, Nantes Université, Université d'Angers, Le Mans Université, Nantes, France

Key Points:

- We combine independent morphostratigraphic and spectral units of Rachmaninoff basin to create geostratigraphic units
- Geostratigraphic units can distinguish volcanic plains and impact melt in contact with each other
- Geostratigraphic units imply a wider distribution of (LRM-composition) impact melt than previously recognized

Supporting Information:

Supporting Information may be found in the online version of this article.

Correspondence to:

J. Wright,
jack.wright@esa.int

Citation:

Wright, J., Zambon, F., Carli, C., Altieri, F., Pöhler, C. M., Rothery, D. A., et al. (2024). A geostratigraphic map of the Rachmaninoff basin area: Integrating morphostratigraphic and spectral units on Mercury. *Earth and Space Science*, *11*, e2023EA003258. https://doi.org/10.1029/2023EA003258

Received 5 SEP 2023
Accepted 5 JAN 2024

Author Contributions:

Conceptualization: Jack Wright, Francesca Zambon, Cristian Carli, Francesca Altieri, Claudia M. Pöhler, David A. Rothery, Carolyn H. van der Bogert
Data curation: Jack Wright, Angelo Pio Rossi
Formal analysis: Jack Wright
Funding acquisition: David A. Rothery, Angelo Pio Rossi, Matteo Massironi, Matthew R. Balme
Investigation: Jack Wright
Methodology: Jack Wright, Francesca Zambon, Cristian Carli, Francesca Altieri, David A. Rothery

Abstract

Geological maps of Earth typically incorporate field observations of rock lithology, structure, composition, and more. In contrast, conventional planetary geological maps are often made using primarily qualitative morphostratigraphic remote sensing observations of planetary surfaces. However, it is possible to define independent quantitative spectral units (SUs) of planetary surfaces, which potentially contain information about surface composition, grain size, and space weathering exposure. Here, we demonstrate a generic method to combine independently derived geomorphic and SUs, using the Rachmaninoff basin, Mercury, as an example to create a new geostratigraphic map. From this geostratigraphic map, we can infer some compositional differences within geomorphic units, which clarifies and elaborates on the geological evolution of the region.

Plain Language Summary

Geological maps of rocks on Earth include information about what landforms the rocks exhibit, what they are made from, their orientation, and more. Many such details require ground observations, but these are generally not available for planetary geological maps, which rely on spacecraft data. Spacecraft images can be used to map planetary surface textures (geomorphology), but they can also be used to measure surfaces' responses to light (reflectance or emission spectra), which contain information about what the surface rocks are made from, their physical properties (e.g., grain size, roughness, porosity), and how long they have been exposed at the surface. We have combined earlier, independent geomorphic and spectral maps of the Rachmaninoff impact basin on Mercury to create a new "geostratigraphic" map that is more like a geological map that could be made of Earth. The new map highlights places that in the original geomorphic map would have been mapped all as a single unit, but are divisible based on spectral variations, attributable to differences in what the rocks are made from. This allows us to reconstruct a more detailed geological history of the region. Our method can be applied to other regions on Mercury and to other planetary surfaces.

1. Introduction

1.1. Planetary Geologic Mapping

Since the early days of planetary geology, geological maps of other planets have been constructed primarily from geomorphically-defined units. These maps have been made mostly using visible image data sets that relay topographic and albedo information. Mappers use such basemaps to describe, demarcate, and determine the stratigraphy of geomorphic units and thus the resultant products should be properly considered as "morphostratigraphic maps." However, geological maps of Earth incorporate multitudinous observations, including those of lithology, composition, structure, and mode of formation to enrich the information communicated by the map (Massironi et al., 2021). Therefore, morphostratigraphic maps of other planetary bodies lack much of the content of geological maps of Earth, limiting their effectiveness as summaries of the geological evolution of those bodies.

However, recent spacecraft missions to Mars and the Moon have had instruments designed to measure the spectra of the surfaces of these worlds (Bibring et al., 2004; Green et al., 2011; Kumar et al., 2009; Murchie et al., 2007),

Project administration: Angelo Pio Rossi, Matteo Massironi, Matthew R. Balme
Supervision: David A. Rothery, Matthew R. Balme, Susan J. Conway
Validation: Jack Wright
Visualization: Jack Wright, Francesca Zambon
Writing – original draft: Jack Wright
Writing – review & editing: Jack Wright, Francesca Zambon, Cristian Carli, Francesca Altieri, Claudia M. Pöhler, Carolyn H. van der Bogert, Angelo Pio Rossi, Matthew R. Balme, Susan J. Conway

allowing for interpretations of their chemical and physical properties. On Mars, geomorphologically-defined map units can have well-defined characteristic spectral signatures (e.g., where these are not obscured by dust) such that Mars mappers routinely incorporate spectral information into their unit descriptions (e.g., Fawdon et al., 2015). The Moon's major terrains are easily distinguished by their morphologies and topographic relationships: the highlands are rugged, densely cratered, relatively high albedo, and high-standing; the maria are smooth, less densely cratered, lower albedo, and they infill topographic lows (Jaumann et al., 2012). Spectral information is important for identifying subdivisions within these major terrains, such as volcanic subunits within lunar maria (Thiessen et al., 2014). In the cases of Mars and the Moon, unit definition therefore often incorporates spectral information from the outset. This, coupled with locally available robotic and human field observations, means that geological maps of Mars and the Moon have greater potential to emulate the richness of geological information typically contained with geological maps of Earth. However, owing to the generally lower spatial resolution of multi- and hyperspectral data sets compared with the monochrome data sets used for studying the geomorphology of a given planetary body, spectral information usually supplements, rather than supersedes, geomorphological information in planetary geological maps.

However, the geomorphology-led approach has weaknesses when applied to other planetary bodies. On small airless bodies, where impact cratering has dominated their geological histories, morphological boundaries are commonly blurred in the available data sets by successive impact ejecta deposits. This diminishes the effectiveness of morphological observations in determining the stratigraphy. To address this problem for Vesta, Yingst et al. (2023) made two maps: the first, a conventional geomorphological map and the second, a spectral unit (SU) map. Yingst et al. (2023) found that spectral data were a more unique discriminator for geological unit definition than geomorphology for Vesta. They then combined these two maps into a hybrid map that retains and displays the important information from each of the constituent maps in order to represent the geological evolution of Vesta as completely as possible.

1.2. Morphostratigraphic Mapping of Mercury

The Mercury Dual Imaging System (MDIS: Hawkins et al., 2007), onboard the MErcury Surface, Space ENvironment, GEochemistry, an Ranging (MESSENGER) mission (Solomon et al., 2007, 2018) collected the first global image data set of Mercury, which is being used to create morphostratigraphic maps that together will cover the entire planet (Blance et al., 2023; Buoninfante et al., 2022; El Yazidi et al., 2021; Galluzzi et al., 2016, 2018; Giacomini et al., 2022, 2023; Guzzetta et al., 2017, 2018; Kinczyk et al., 2020; Lennox et al., 2021; Lewang et al., 2018; Malliband et al., 2022; Man et al., 2023; Mancinelli et al., 2016; Ostrach et al., 2020; Pegg, Rothery, Balme, et al., 2021; Prüsse et al., 2020; Wright et al., 2019). The globally recognized morphostratigraphic units on Mercury that make up such maps include: intercrater plains, which are level-to-gently rolling rough-textured plains with a high density of superposing secondary craters; smooth plains, which are usually level plains with a relatively smooth texture, a low density of superposing craters, and sharp contacts with adjacent units; intermediate plains, which have a texture intermediate in roughness between intercrater and smooth plains, and; various units associated with Mercury's impact craters, such as smooth crater floor deposits that are geomorphologically indistinguishable from smooth plains (Denevi et al., 2013; Galluzzi et al., 2018; Kinczyk et al., 2020; Trask & Guest, 1975; Whitten et al., 2014). In line with the longstanding practice in planetary geology, these units are defined based on their appearance only (Hargitai & Naß, 2019), without prescribing how each unit formed (cf. smooth plains and lava plains), and so it is common for interpretations of different exposures of a given morphostratigraphic unit to have different interpretations. Ideally, further data sets could be used to disambiguate these units.

Mercury is less well-explored than Mars and the Moon, so these maps rely on the geomorphology-led approach. Until landed Mercury science commences (Byrne et al., 2021; Ernst et al., 2022), it seems unlikely that lithological or definitive rock origin information could be included in a geological map of Mercury, for example, the geological map of H05 (Wright et al., 2019). Recently, structural measurements of the shallowly dipping faults associated with some lobate scarps on Mercury have been made (Galluzzi et al., 2015; Pegg, Rothery, Conway, & Balme, 2021), but the remote sensing techniques used rely on rare cross-cutting relationships, and so cannot be employed widely enough to adorn Mercury maps with strike and dip measurements.

1.3. Spectral Mapping of Mercury

MESSENGER did, however, make global measurements pertaining to Mercury's surface composition, including major element measurements using X-ray (Nittler et al., 2020, 2023) and gamma-ray spectroscopy (Evans et al., 2012). Major element maps have been successfully used to delineate geochemical terranes on Mercury (Peplowski et al., 2015; Peplowski & Stockstill-Cahill, 2019; Vander Kaaden et al., 2017; Weider et al., 2015) and some of these do correspond well with the boundaries of morphostratigraphic units, such as the smooth plains of Caloris Planitia and Borealis Planitia (Weider et al., 2015). However, owing to the generally low spatial resolution of MESSENGER X-ray and gamma ray spectroscopic data we can currently infer only global-scale compositional variations, which would not greatly enhance information contained within most quadrangle or local-scale geological maps.

Multispectral observations by MDIS were made at a consistently comparable spatial resolution (i.e., a few hundred meters per pixel) to the monochrome basemaps used for morphostratigraphic mapping of Mercury's quadrangles (Galluzzi et al., 2021). MDIS imaged Mercury in the ~430–1,000 nm range (visible and near-infrared: VNIR), sampling the uppermost millimeter of the surface regolith. At least the uppermost meter of Mercury's regolith should be vertically well-mixed by impact gardening (Langevin, 1997) such that reflectance spectra are representative of the underlying bedrock (Evans et al., 2012), except where fresh ejecta or volatile elements have been deposited (Rothery et al., 2010).

Surface spectral variations on Mercury are caused by differences in composition, physical properties (e.g., grain size), and space weathering exposure (Domingue et al., 2014; Pieters & Noble, 2016; Riner & Lucey, 2012). Mercury's reflectance spectra in the VNIR typically lack definitive absorption features (Murchie et al., 2015) most likely because of the deposition of submillimeter particles, including but not limited to metallic iron, by space weathering processes. The presence of such particles masks the spectral signature of the primary surface material, making mineral identification highly inconclusive (Domingue et al., 2014). However, there is some evidence for weak absorption features associated with Mercury's hollows and low-reflectance material. Hollows are rimless, geologically recent depressions tens of kilometers across and tens of meters deep most commonly found on crater floors hypothesized to be formed by surface volatile loss (Blewett et al., 2011; Lucchetti et al., 2018; Thomas et al., 2014). Low-reflectance material is hypothesized to be graphite-rich remnants of Mercury's primary crust (Klima et al., 2018; Vander Kaaden & McCubbin, 2015). Furthermore, many putative pyroclastic deposits on Mercury exhibit a downturn toward UV wavelengths (i.e., steeper UV slopes: Barraud et al., 2021; Goudge et al., 2014). Therefore, the overall shapes of the spectra vary on spatial scales such that characteristic spectra of certain geological features can be identified (Zambon et al., 2022).

To investigate the spectral variability within the Hokusai quadrangle (H05) of Mercury, Zambon et al. (2022) created a ~450 m/pixel mosaic of H05 using multispectral cubes created using all eight MDIS wide-angle camera filters in the ~430–1,000 nm wavelength range. They defined four spectral indices (reflectance at 750 nm, spectral slope between 430 and 560 nm, spectral slope between 750 and 1,000 nm, and the full spectral range slope between 430 and 1,000 nm) to quantify the spectral variability. They selected thresholds to separate spectral index values into seven intervals: very low, low, intermediate low, intermediate, intermediate high, high, and very high. They determined the intervals for each spectral index in every pixel in the mosaic and unique combinations of spectral index intervals became SUs. They merged many SUs with only slightly differing spectral index interval combinations. Ultimately, they identified 11 distinct SUs within H05 (simply numbered SU1–SU11: the numbers used have no additional meaning beyond designating the SU), some of which are readily attributable to geological features (Zambon et al., 2022) but a formal integration of their SU map and the morphostratigraphic map of H05 (Wright et al., 2019) was left for a future work.

1.4. Integration of Morphostratigraphic and Spectral Units for H05

In this study our aim was to create new "geostratigraphic units" (*sensu* Massironi et al., 2021) where spectral information augments the descriptions and contacts of morphostratigraphic units by fusing the information contained within the Zambon et al. (2022) and Wright et al. (2019) maps. To achieve this, we needed to select a study area within H05 with a diversity of both morphostratigraphic units and SUs so that their fusion would produce additional geological insights. For example, we wanted to investigate the possibility of distinguishing smooth impact melt and volcanic plains in contact with each other, which cannot be separated on purely geomorphological grounds. We also wanted to establish if the SUs can tell us more about the pre-impact stratigraphy. For a ballistically emplaced impact ejecta deposit, which becomes thinner with increasing distance from the crater center (Housen et al., 1983), the distal ejecta eventually becomes critically thin (on the order of meters: Langevin, 1997) and its spectral signature should be mixed with that of the underlying material by impact gardening, allowing inferences about the subsurface stratigraphy to be made.

For this task we selected Rachmaninoff basin and its surroundings, from the southeast part of the H05 quadrangle. Rachmaninoff is a 290 km-diameter peak ring basin with a relatively undegraded appearance and an ejecta deposit that superposes nearby smooth plains (Marchi et al., 2011; Prockter et al., 2010; Wright et al., 2019; Wright, Byrne, & Rothery, 2021), indicating that the impact postdates the end of large-volume effusive volcanism in the region (Byrne et al., 2016). Rachmaninoff contains low-reflectance material (Denevi et al., 2009; Klima et al., 2018; Marchi et al., 2011; Prockter et al., 2010), which contrasts starkly with the high-reflectance, redder spectral signature of Nathair Facula, the largest putative explosive volcanic deposit on Mercury (Barraud et al., 2021; Besse et al., 2020; Kerber et al., 2011; Leon-Dasi et al., 2023; Rothery et al., 2021), nearby to the northeast. The interior of Rachmaninoff contains Mercury's lowest surface elevation (Becker et al., 2016) and the planet's thinnest crust (Beuthe et al., 2020). Thus, the low-reflectance material exposed by Rachmaninoff in its peak ring, walls, floor, and ejecta most likely comes from the base of Mercury's crustal stratigraphy. Low reflectance blue plains (Denevi et al., 2009) are found in the annulus between the peak ring and the crater rim, as well as small patches beyond the crater rim. These exterior patches are most probably impact melt (Wright et al., 2019; Wright, Byrne, & Rothery, 2021) although they are indistinguishable from smooth plains of probable volcanic origin elsewhere on Mercury on purely geomorphological grounds and thus Wright et al. (2019) had to group these plains units despite their different probable origins. The gap in Rachmaninoff's peak ring is indicative of an oblique impact (Gault & Wedekind, 1978) with a downrange direction toward the south. This is broadly consistent with the concentration of probable crater rim exterior impact melt ponds between southern and western azimuths, as impact melt is preferentially deposited downrange (Gault & Wedekind, 1978). If Rachmaninoff's impact melt has a distinct spectral signature, then we wanted to test if this spectral signature coincides with the geomorphic evidence for impact melt. Contrasting high-reflectance red plains cover Rachmaninoff's floor within its peak ring and extend beyond the southern gap in the ring, terminating in faculae (including Suge Facula: Prockter et al., 2010; Wright, Byrne, & Rothery, 2021). These smooth plains are hypothesized to be volcanic in origin (Chapman et al., 2012; Prockter et al., 2010; Wright, Byrne, & Rothery, 2021), and so it is important to investigate if Rachmaninoff's younger volcanic plains are spectrally different from the nearby, older, larger-volume volcanic plains.

We expect space weathering exposure effects to be mostly uniform over the study area because, with the exception of some superposing bright crater rays from the Hokusai impact crater, and possibly some faculae, most of the materials in the study area are at least 1 Gyr old, as so will be covered with optically mature regolith (Neish et al., 2013). Crater rays on Mercury are hypothesized to have high albedos because of exhumation of optically immature material by secondary cratering along their lengths and have been dated to be less than 230 Myr old (Banks et al., 2017)—much younger than most of the study area. Steep slopes, such as those forming crater walls, are the most probable places to exhibit space weathering exposure-induced spectral contrasts. This is because mass wasting on slopes inhibits regolith accumulation and exposes fresh material.

2. Materials and Methods

2.1. Data

We used the publicly available vector mapping features for the morphostratigraphic map of H05 (Wright, Rothery, et al., 2021), which have undergone minor revisions since the original publication of the Wright et al. (2019) map, and the SU map by Zambon et al. (2022) as inputs for data fusion. Briefly, the Wright, Rothery, et al. (2021) files contain separate line vectors for the morphostratigraphic contacts and other linear features, and polygon vectors for the morphostratigraphic units and surface features (e.g., faculae). Figure 1 shows these data in our Rachmaninoff basin study region.

2.2. Methods

We used Esri ArcMap 10.6 to perform the data fusion in the same Lambert conformal conic projection (Snyder, 1987) for H05 used by Wright et al. (2019) and Zambon et al. (2022) to ease comparisons between the input maps and the data fusion product. We began data fusion by digitizing the boundaries between SUs in the SU

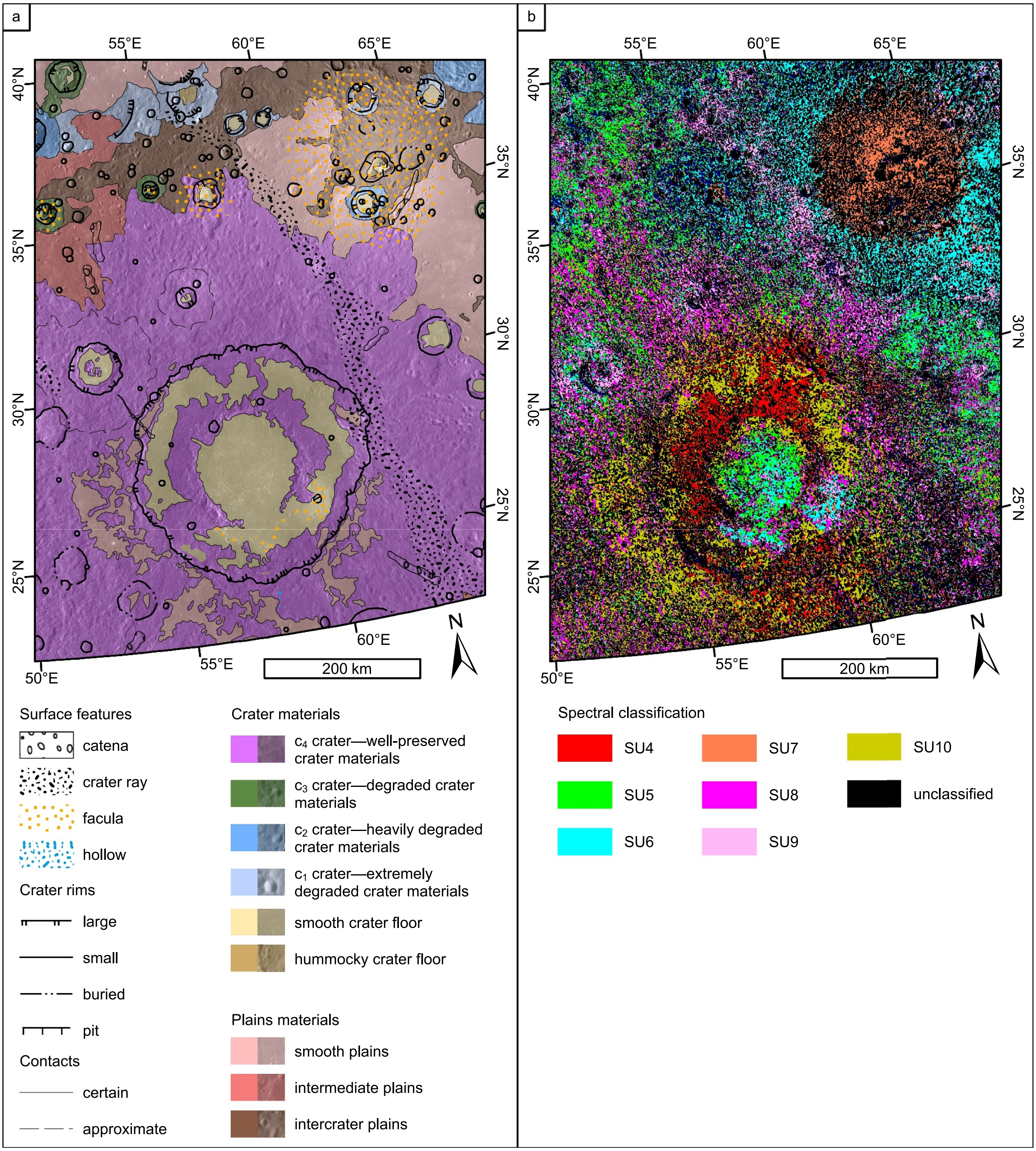

Figure 1. Inputs for data fusion. (a) Simplified morphostratigraphic map of the Rachmaninoff basin study region (after Wright, Rothery, et al., 2021). (b) Spectral unit (SU) map of the Rachmaninoff basin study region (after Zambon et al., 2022). Note that SUs 1–3 and 11 do not form areally significant contiguous units in the study region and hence are not shown in the key.

raster (Figure 2a) so that we could compare these "spectral contacts" with the H05 morphostratigraphic contacts (Wright, Rothery, et al., 2021). Spectral contacts were digitized at a scale of 1:1,000,000. We chose a small digitization scale (*sensu* Fuechsel, 2023) so that we could easily summarize the spectral information and exclude extraneous details, such as pixel-scale SUs (1–3 and 11). We compared the spectral contacts and morphostratigraphic contacts of H05 by overlaying them. We assessed the geologic origins of resultant geostratigraphic

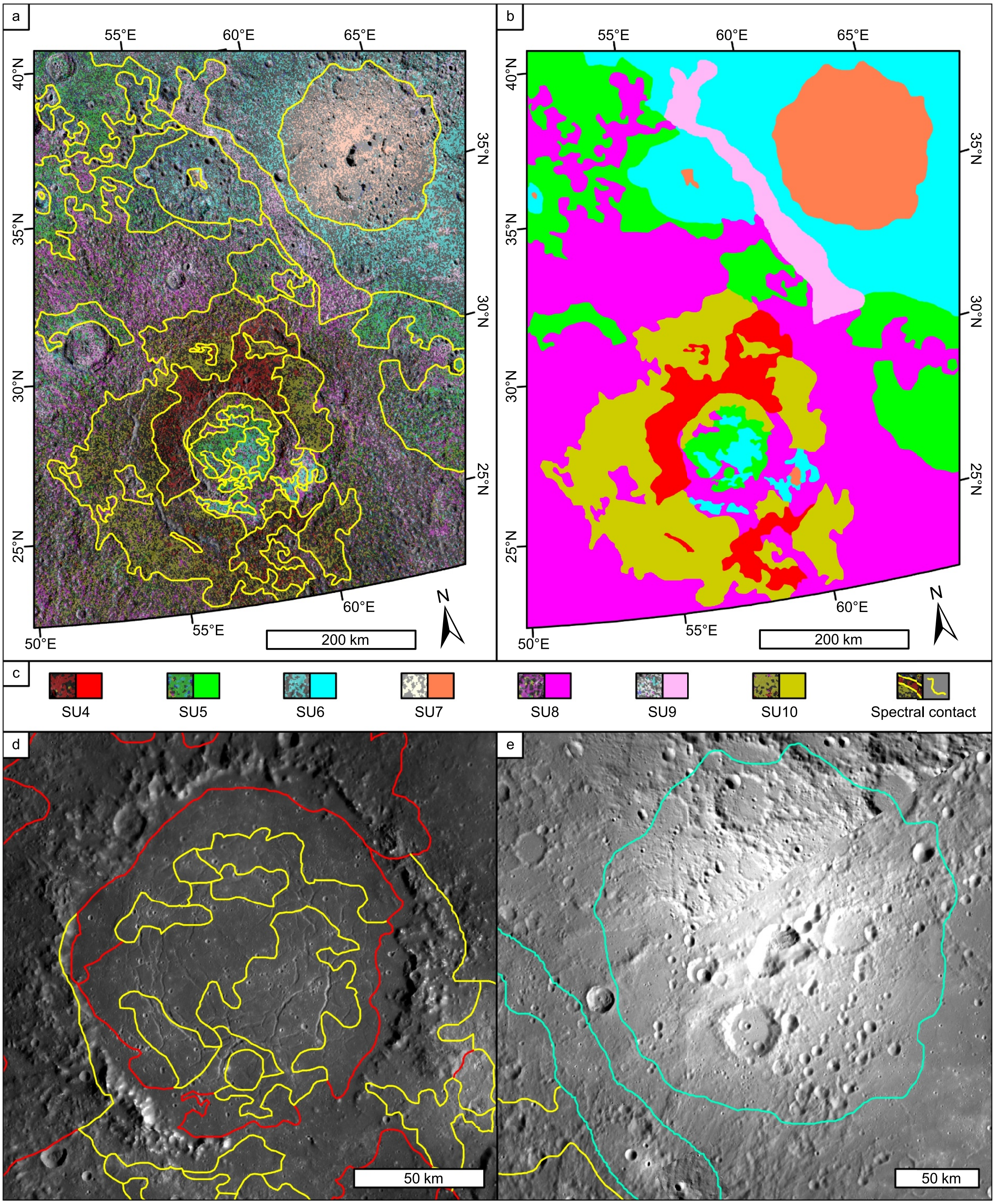

Figure 2. Spectral contacts method. (a) Rachmaninoff study area with spectral unit (SU) map by Zambon et al. (2022) overlain on the ~166 m/pixel monochrome basemap. Areas dominated by different SUs are separated by spectral contacts (yellow lines). (b) Vectorized SUs. (c) Key for panels (a) and (b). (d) Spectral contacts with Rachmaninoff's peak ring. Spectral contacts in yellow exist wholly within a morphostratigraphic unit mapped by Wright, Rothery, et al. (2021). Spectral contacts shown in red correspond entirely or partially with morphostratigraphic contacts mapped by Wright, Rothery, et al. (2021). This shows that there is SU diversity within the smooth plains within Rachmaninoff, and that some spectral diversity within this view correlates with geomorphic features. (e) Nathair Facula. Spectral contacts shown in cyan correspond closely with the outlines of surface features such as crater rays (lower left) and faculae (center) mapped by Wright, Rothery, et al. (2021).

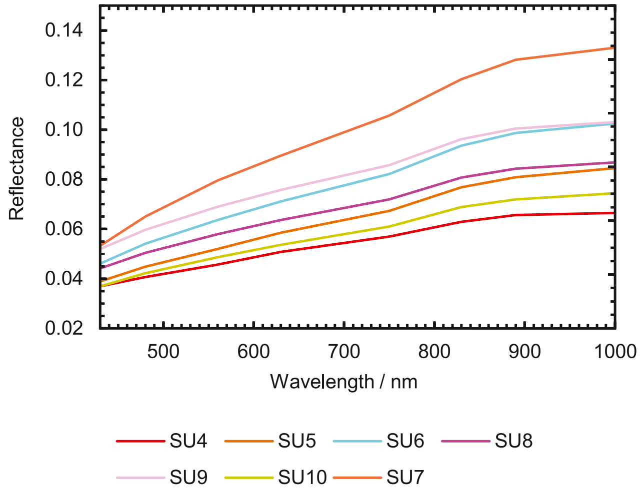

Figure 3. Mean reflectance spectra of spectral units from Zambon et al. (2022) that are spatially extensive in the mapping area.

units by examining them in the ~166 m/pixel MDIS monochrome basemap of Mercury and by looking at higher resolution individual MDIS images. We show the mean reflectance spectra, taken from Zambon et al. (2022) of the spatially extensive SUs found within the mapping area in Figure 3.

We found that a given spectral contact could exhibit one of three spatial relationships with the morphostratigraphic linework: (a) the spectral contact closely coincides with a morphostratigraphic contact (Figure 2d); (b) the spectral contact cuts one or more morphostratigraphic units (Figure 2d), or; (c) the spectral contact closely coincides with the boundary of a surface feature (SUs 7 and 9; Figure 2e). We interpret that spectral contacts that closely coincide with morphostratigraphic contacts represent the boundary between geomorphically distinct units that could be spectrally distinct because of either grain size or composition, such as the boundary between Rachmaninoff's peak ring and probable volcanic material on the basin floor (Figure 2d; Prockter et al., 2010). We interpret that spectral contacts that cut morphostratigraphic contacts indicate compositional variation, since the effects of grain size and space weathering should be equal throughout a morphostratigraphic unit, except where the spectral boundary coincides with a break in topographic slope within a morphostratigraphic unit, in which case regolith optical maturity might be responsible. Such variation could be surficial, caused for example, by the superposition of crater rays on the unit, or could reflect real compositional variation within bedrock, such as intermingled impact melt and volcanic plains within the same smooth plains unit. Therefore, SUs can correspond to surficial units or morphostratigraphic units. We are interested in bedrock geostratigraphic units, rather than surficial spectral responses and so we removed spectral contacts that, when viewed in the overlay, clearly corresponded with the boundaries of surficial features in preparation for the creation of the geostratigraphic units. SU7 and SU9 coincide precisely with Nathair Facula, a surficial deposit putatively of pyroclastic origin, and a distal ejecta ray from Hokusai crater, respectively. We added this information to the surface features vector file, but we do not discuss these surficial spectral responses further here.

To fuse the SUs and morphostratigraphic units, we created a new "geostratigraphic contacts" vector feature (Figure 4). We copied the Wright, Rothery, et al. (2021) morphostratigraphic contacts into the geostratigraphic contacts so that they could act as a framework for purely spectral contacts to be added to. We did this because: (a) the morphostratigraphic units were mapped at higher spatial resolution than the SUs and thus the morphostratigraphic contacts are placed more precisely, and; (b) we wanted the morphostratigraphic observations to be the primary source of stratigraphic information and for this to be augmented by spectral information. We created the remaining geostratigraphic contacts by tracing spectral contacts within morphostratigraphic units and adding these purely spectral geostratigraphic contacts to the initial morphostratigraphic-origin contact framework. To distinguish the new, purely spectral geostratigraphic contacts from morphostratigraphic-origin geostratigraphic contacts, we used a green, dot-dash line symbol for the spectral contacts, and we retained the black line symbols used by Wright et al. (2019) for the morphostratigraphic-origin contacts (Figure 5). We created geostratigraphic units by using the geostratigraphic contacts and the study area outline as the inputs for the "Feature Class to Polygon" tool. Each resultant geostratigraphic unit polygon is therefore the intersection of one morphostratigraphic unit and one SU. We created new names for each geostratigraphic unit by appending its SU number (Zambon et al., 2022) as a superscript to its morphostratigraphic code (Wright, Rothery, et al., 2021). For example, where the morphostratigraphic unit smooth plains (sp) and spectral unit 6 (SU6) coincide, the resultant geostratigraphic unit is sp^6.

Although not every morphostratigraphic unit intersected with every SU (see key in Figure 5), the geostratigraphic map contains 31 units, compared with 10 in the morphostratigraphic map (Wright et al., 2019). Representing these units on the map, while communicating the geomorphic and spectral information simultaneously, is cartographically challenging. We opted to apply a modified version of the morphostratigraphic unit color scheme of Wright et al. (2019) to each geostratigraphic unit where the brightness of the color is changed according to the corresponding SU. Five SUs occur in geostratigraphic bedrock units in the study area, which we rank here in descending order of reflectance at 750 nm: SU6, SU8, SU5, SU10, SU4 (Zambon et al., 2022). We assigned the original morphostratigraphic unit color from Wright et al. (2019) to geostratigraphic units exhibiting SU8.

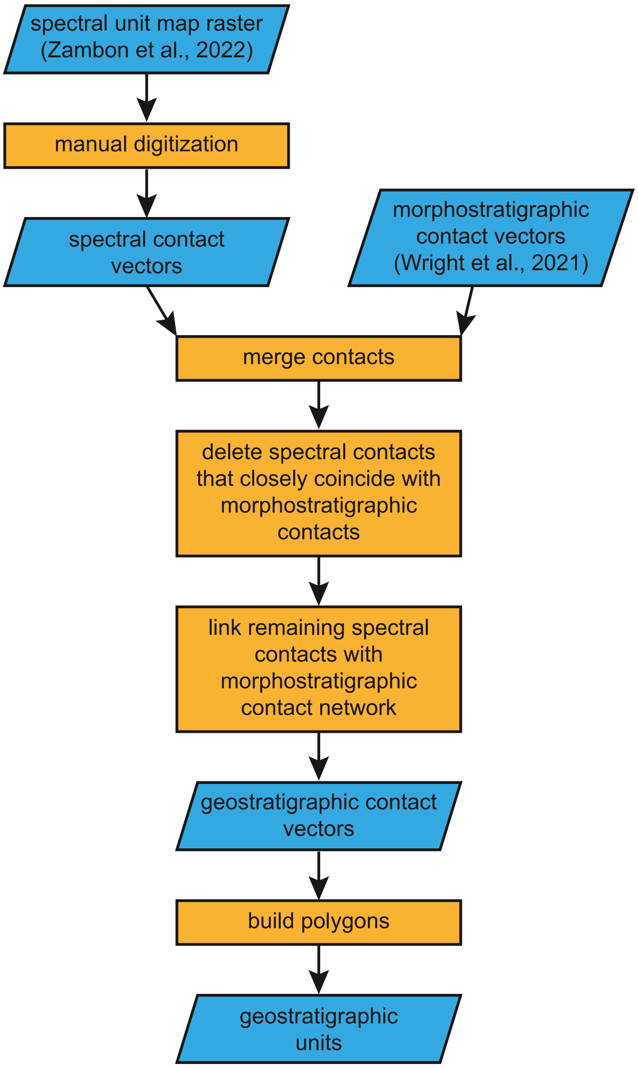

Figure 4. Flowchart outlining the steps we followed to generate geostratigraphic units.

Zambon et al. (2022) found that, across H05, SU8 is an intermediate SU and they suggested that it is a mixture of other brighter and darker endmember SUs. SU8 is exhibited by all the morphostratigraphic units in the study region but it has no strong affinity for any given morphostratigraphic unit. Geostratigraphic units with SU6 were symbolized with a color 7% lighter in Hue, Saturation, Lightness (HSL) space (see Yan et al., 2021 and references therein) than their corresponding Wright et al. (2019) morphostratigraphic unit symbol, to communicate that these are higher reflectance units within the study area. Geostratigraphic units with SU5, SU10, and SU4 were symbolized with colors 7%, 14%, and 21% lower in Lightness than their corresponding Wright et al. (2019) morphostratigraphic unit color, respectively, to communicate in particular that SU10 and SU4 are the lowest reflectance SUs in the whole quadrangle (Zambon et al., 2022). Indeed, SU4 corresponds with Mercury's low-reflectance material (Zambon et al., 2022), which is the darkest surface material on the whole planet (Denevi et al., 2009; Klima et al., 2018). Our chosen 7% lightness interval between the colors of geostratigraphic units of the same original morphostratigraphic unit but different SUs is a compromise to allow adequate distinction between the geostratigraphic unit colors without the SU6-bearing unit colors appearing so washed out as to be indistinguishable (0% and 100% lightness yield black and white irrespective of hue: see Yan et al., 2021 and references therein).

We developed this approach to cope with the potentially high number of unique morphostratigraphic and SU combinations. Unfortunately, this approach might not be practical for a map containing a large number of SUs, since the geostratigraphic units with the highest and lowest reflectance SUs could be too washed out and darkened, respectively, to be distinguished on the map. In such cases, it might be necessary to reduce the number of units in the map by focusing on the minimum required to address the science question the map was created to answer, or to adopt a new high-contrast color scheme. Nevertheless, we found that our approach worked well for our study area.

3. Results

Our geostratigraphic map of the Rachmaninoff basin and its surroundings (Figure 5: see Main Map in Supporting Information S2) communicates important geological information that could not be captured by the morphostratigraphic map (Wright et al., 2019), as detailed in the following subsections and summarized in Table 1.

Here we describe the new geostratigraphic units and, where possible, provide updated interpretations for their origins. In our method, the SUs augment the morphostratigraphic units of Wright et al. (2019), who for their quadrangle-scale map of H05 lumped crater ejecta, wall, and central uplift materials into a single unit. At the larger scale of our map, with the addition of the SU information, we have been able to subdivide many former morphostratigraphic units. In the subsections that follow, we provide descriptions and interpretations of our new geostratigraphic units grouped by their parent morphostratigraphic unit. Each group begins with a description of the parent morphostratigraphic unit based on those of Wright et al. (2019). We arbitrarily list the geostratigraphic units within each grouping in descending order of reflectance at 750 nm.

3.1. Plains Units

3.1.1. Smooth Plains (sp)

These are sparsely cratered plains that present sharp contacts with adjacent units (Wright et al., 2019). They mostly extend between craters, but areally significant patches are found outside Rachmaninoff's crater rim, particularly counterclockwise between western and southern azimuths.

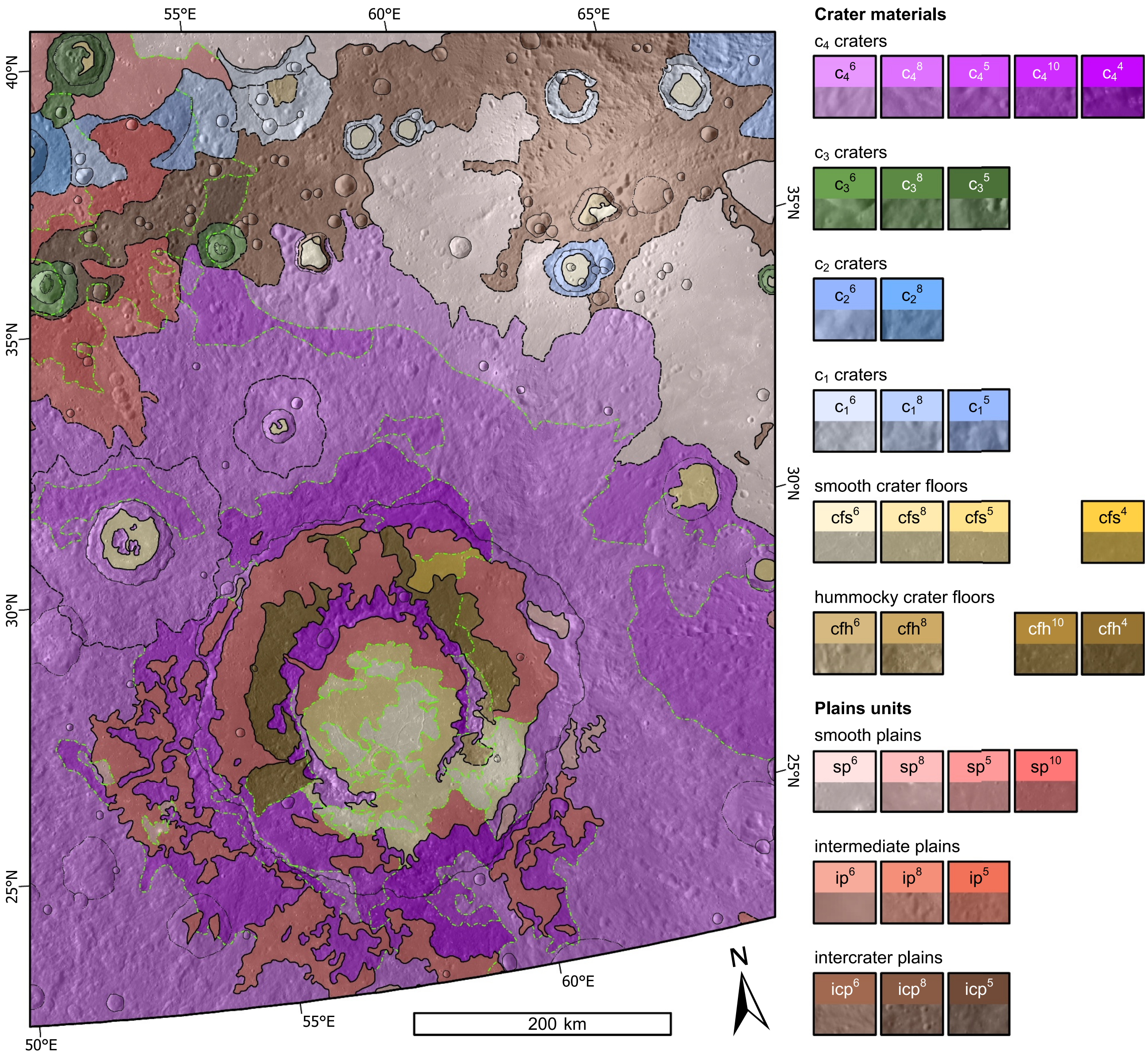

Figure 5. Simplified geostratigraphic map of Rachmaninoff basin showing geostratigraphic units and contacts. For the full version of this map, see the map sheet in Supporting Information S2.

sp^6—Extensive smooth plains belonging to Borealis Planitia, which extends into the northernmost part of the mapping area, and minor plains west and southeast of Nathair Facula.

Interpretation: Effusive volcanic plains formed toward the end of Mercury's large-volume eruptive history (Byrne et al., 2016).

sp^8—Small patches of smooth plains perched in Rachmaninoff's proximal impact ejecta.

Interpretation: Ponded Rachmaninoff impact melt composed of SU8-bearing (icp^8?) target material.

sp^5—Southernmost smooth plains of Borealis Planitia found in contact with low-reflectance crater materials.

Interpretation: Thin effusive volcanic plains (sp^6) whose original spectral signature has been laterally mixed with SU5-bearing crater materials nearby and vertically mixed with underlying SU5-bearing plains (icp^5?). Our hypothesis that sp^5 has a mixed spectral signature is consistent with the distribution of SU5 throughout H05.

Zambon et al. (2022) found that SU5 is not associated with any one terrain type in H05. Instead, it is found along the boundaries between other major SUs and it has intermediate values of all spectral parameters.

sp^{10}—Smooth plains within Rachmaninoff's northern crater floor and proximal impact ejecta in the northwest, southwest and southeast where it is interspersed with $c_4{}^{10}$.

Interpretation: We interpret sp^{10} as Rachmaninoff impact melt that has been able to pond. The close spatial association between sp^{10} and SU4-bearing materials might suggest that sp^{10} formed by impact melting of low-reflectance material.

3.1.2. Intermediate Plains (ip)

These are plains with a texture intermediate in roughness between smooth plains and intercrater plains. They are characterized by hummocky terrain composed of degraded crater rims with intervening low-lying regions with smooth, level surfaces existing between impact craters. It has been suggested that this unit in this region represents intercrater plains that have been partially inundated by smooth plains (Wright et al., 2019; Wright, Byrne, & Rothery, 2021).

ip^{6}—A very minor unit with a single exposure at the northwestern edge of the map, adjacent to a crater containing a minor facula.

Interpretation: Effusive volcanic plains (sp^{6}-type?) that have incompletely buried the underlying intercrater plains. A superposing SU6-bearing facula either imparts, or reinforces an original, SU6 spectral signature.

ip^{8}—A moderately extensive unit beyond Rachmaninoff's northwestern ejecta deposit. Very similar in appearance and distribution to ip^{5}, with the spectral signature (SU8 rather than SU5) being the only significant difference.

Interpretation: Thin effusive volcanic plains (sp^{6}-type?) that have incompletely buried the underlying, darker intercrater plains, and whose original spectral signature has been laterally mixed with SU8-bearing crater materials nearby and vertically mixed with underlying SU8-bearing plains (icp^{8}?).

ip^{5}—A moderately extensive unit beyond Rachmaninoff's northwestern ejecta deposit. Very similar in appearance and distribution to ip^{8}, with the spectral signature (SU5 rather than SU8) being the only significant difference.

Interpretation: Thin effusive volcanic plains (sp^{6}-type?) that have incompletely buried the underlying, darker intercrater plains, and whose original spectral signature has been laterally mixed with SU5-bearing crater materials nearby and vertically mixed with underlying SU5-bearing plains (icp^{5}?).

3.1.3. Intercrater Plains (icp)

These are heavily cratered plains with a rough, hummocky texture, extending between impact craters (Wright et al., 2019).

icp^{6}—Extensive cratered plains found in the north of the mapping area in contact with sp^{6} and/or with superposing faculae.

Interpretation: Plains formed mostly from an earlier stage of effusive volcanism than formed the smooth plains (Whitten et al., 2014), perhaps with some incorporated impact ejecta, but whose original spectral signature has been overprinted by that of faculae and sp^{6} by impact gardening from surrounding units.

icp^{8}—Minor cratered plains with SU8 found northwest of Rachmaninoff's $c_4{}^{8}$ impact ejecta.

Interpretation: Old effusive volcanic plains that pre-date smooth plains, probably also incorporating ancient impact ejecta. Very similar in appearance and distribution to icp^{5}, with the spectral signature (SU8 rather than SU5) being the only significant difference.

icp^{5}—Minor cratered plains with SU5 found northwest of Rachmaninoff's impact ejecta.

Interpretation: Old effusive volcanic plains that pre-date smooth plains, probably also incorporating ancient impact ejecta. Very similar in appearance and distribution to icp^{8}, with the spectral signature (SU5 rather than

SU8) being the only significant difference. icp^5 could be the same material as icp^8 but with a different spectral response because of physical properties affecting space weathering.

3.2. Crater Materials

3.2.1. Well-Preserved Crater Materials (c_4)

These craters have sharp and complete rims, undegraded and well-defined wall terraces where present, and sharp internal uplift peaks where present. Their wall-floor and distal ejecta contacts are distinct. Their impact ejecta remains strongly radially textured up to around one crater diameter from the crater rim, but bright crater albedo rays are absent. Radial catenae (secondary crater chains) are often present (Wright et al., 2019).

$c_4{}^6$—These materials have two settings. First, they occur extensively north of Rachmaninoff. Here they have a feather-like texture that radiates from Rachmaninoff and becomes interspersed with a smoother texture with increasing distance from the basin. They encompass many impact craters with muted appearances, and host very few fresh craters.

Second, these materials occur as areally limited outcrops of rugged material closely associated with faculae within the annulus between Rachmaninoff's peak ring and crater rim.

Interpretation: We interpret these materials as Rachmaninoff ejecta and uplift that have been affected by pre-existing or subsequent volcanic spectral signatures. We interpret the first type as distal Rachmaninoff ejecta superposing sp^6. This is consistent with the unit's feather-like texture that becomes smoother closer to the smooth plains contact, which indicates ballistically emplaced ejecta that decreases in thicknesses away from the source crater's rim. The muted craters have been mantled by $c_4{}^6$, whereas the small number of fresh craters that superpose it indicate that $c_4{}^6$ is one of the youngest units in the mapping area. We believe that the Rachmaninoff ejecta here in isolation would exhibit the SU of other nearby Rachmaninoff materials (mostly likely SU8), but here it is sufficiently thin that its natural spectral signature has been overridden by the underlying sp^6 that has been incorporated into it by impact gardening.

We interpret the second type as rugged Rachmaninoff peak ring and crater rim elements that have been mantled by faculae. These faculae, results of post-Rachmaninoff putative explosive volcanic activity, have overprinted the original crater materials SU with SU6.

$c_4{}^8$—This unit has two types, each with a separate setting. The first type is found beyond the rims of Rachmaninoff and two smaller craters northwest of Rachmaninoff. In the case of Rachmaninoff, this unit has a similar texture to the radial, feather-like expression of $c_4{}^6$. This crater-radial texture is weaker around the smaller craters northwest of Rachmaninoff.

The second type is rugged material that forms the crater walls and central uplift of Rachmaninoff and the two craters northwest of it.

Interpretation: We interpret these materials as Rachmaninoff ejecta and uplift that exhibit the SU of the target material. Again, we interpret the first type as ballistically emplaced ejecta. This is the most areally extensive of Rachmaninoff's ejecta materials, so we believe that it is unlikely that these materials have had their original SU altered by mixing with other geostratigraphic units. Therefore, we interpret SU8 as the original SU of the target material of the Rachmaninoff impact, which has remained unchanged by the impact. The second type is material uplifted from the subsurface probably sourced from the same compositionally distinct substratum as the impact ejecta. Rachmaninoff superposes all three plains units in the mapping area, but smooth and intermediate plains are relatively minor compared with intercrater plains, so we suggest that icp^8 is the most likely target material.

$c_4{}^5$—These are materials that occur around Rachmaninoff and around one crater in Rachmaninoff's northwestern ejecta. It has the same feather-like texture as $c_4{}^8$.

Interpretation: We interpret this unit as ballistically emplaced impact crater ejecta. Zambon et al. (2022) interpreted SU5 as being a mixture between SU9, correlated with albedo rays from the Hokusai impact crater, and other SUs. However, $c_4{}^5$ is not coincident with distal Hokusai rays in the study area visible in the MDIS enhanced color mosaic. Therefore, we interpret $c_4{}^5$ as being freshly excavated material with an original SU5 association. As with $c_4{}^8$, the target material is uncertain, but we suggest that icp^5 is the most likely candidate.

c_4^{10}—These materials are exclusively found less than 100 km from Rachmaninoff's rim, predominantly outside the crater from the northwest counterclockwise around to the southeast. Outside the crater rim, the unit resembles c_4^{8} in that it has a feather-like texture that radiates from Rachmaninoff interspersed with sp^{10}. Inside the crater rim, the unit is characterized by rugged material also interspersed with sp^{10}.

Interpretation: We interpret c_4^{10} as crater wall, floor, and ejecta materials that have incorporated Rachmaninoff impact melt (sp^{10}). This is consistent with the smooth material interspersed between the rougher c_4^{10} textures. Because of the abundance of low-reflectance material mapped where this unit is exposed (Klima et al., 2018), we hypothesize that this unit is specifically composed of impact-melted low-reflectance material.

c_4^{4}—This unit is exclusive to Rachmaninoff and it is the most important unit in the crater's peak ring. c_4^{4} is also found in the southern crater rim, with some also found on the crater floor and some among the patches of smooth material beyond the crater rim. In the peak ring this unit forms narrow, discontinuous chains of peaks. On the crater floor adjacent to the peak ring and crater rim the unit constitutes disorganized hummocky terrain. Where this unit occurs immediately beyond the first terrace that delineates Rachmaninoff's crater wall, it resembles c_4^{8} texturally.

Interpretation: We interpret c_4^{4} as material excavated by Rachmaninoff from a deeper substratum than the c_4^{8} source, based on its location in the center of the crater. c_4^{4} is coincident with low-reflectance material, most commonly exposed in impact craters (Denevi et al., 2009; Klima et al., 2018), which is consistent with a source toward the base of Mercury's crustal stratigraphy. We interpret the disorganized, hummocky c_4^{4} around the base of the peak ring and crater rim as mass wasting debris from these sources.

3.2.2. Moderately Degraded Crater Materials (c_3)

These craters have complete but muted crater rims and central uplift and they also host some superposing craters. Their ejecta is discernible but not strongly textured, it extends less than one crater diameter from the crater rim and catenae are rare. Their wall terraces are somewhat degraded. These craters can be embayed by smooth plains (Wright et al., 2019).

c_3^{6}—These impact crater materials encompass crater floors, walls, and ejecta and are superposed by faculae or occur on sp^{6}.

Interpretation: As with c_4^{6}, we interpret these materials as having had their natural spectral signature masked by SU6 either from later explosive volcanic eruptions depositing superposing SU6 materials or embayment by sp^{6} and subsequent spectral mixing from space weathering.

c_3^{8}—This geostratigraphic unit occurs in distal ejecta of a single crater in the northwest corner of the mapping area.

Interpretation: Crater materials that are excavated pre-smooth plains target material. This target material was probably what is observable today as icp^{8}.

c_3^{5}—Occurs in various crater materials, including the distal ejecta of some craters that contain faculae toward their centers.

Interpretation: Degraded crater materials that have experienced either of the following: (a) superposition by explosive volcanic deposits that either have a primary SU5 spectral signature, or (b) excavation from an original SU5-bearing substratum (icp^{5}?). Based on our interpretation that the smooth plains of Borealis Planitia in this area are thin and therefore exhibit sp^{5}, rather than their more characteristic sp^{6}, because of mixing with the underlying materials, we prefer the second of these two explanations.

3.2.3. Very Degraded Crater Materials (c_2)

These craters have rims that are mostly complete but are greatly subdued. Central uplift is formed of minor hummocks or completely absent. These craters are commonly embayed by plains and superposed by other craters such that distal ejecta is mostly absent for all but the largest craters (Wright et al., 2019).

$c_2{}^6$—Occurs in craters that are either directly superposed by Nathair Facula or are located just beyond it. These craters are also embayed by sp^6.

Interpretation: Crater materials that have had their natural spectral signature masked by mixing with SU6 volcanic materials associated with distal Nathair Facula deposits and impact gardening from embaying sp^6.

$c_2{}^8$—Occurs in the walls and ejecta of a single crater in the northwest of the mapping area.

Interpretation: Crater materials that are excavated pre-smooth plains target material. This target material was probably what is observable today as icp^8.

3.2.4. Extremely Degraded Crater Materials (c_1)

These craters have rims that are incomplete and exist as minor rises in the topography rather than easily delineated crests. The original crater floor units have often been buried by external plains units. The impact ejecta is present only in the largest examples (Wright et al., 2019).

$c_1{}^6$—Occurs in craters superposed by Nathair Facula or located just beyond it. Also occurs in craters embayed by sp^6.

Interpretation: Crater materials that have had their natural spectral signature masked by mixing with SU6 volcanic materials associated with distal Nathair Facula deposits and impact gardening from embaying sp^6.

$c_1{}^8$—Occurs in the ejecta of a single crater in the northwest of the mapping area. This crater is surrounded by smooth plains and intermediate plains units.

Interpretation: Crater materials that are excavated pre-smooth plains target material. This target material was probably what is observable today as icp^8.

$c_1{}^5$—Occurs in the crater rim and floor of a crater in the northwest of the mapping area. This crater is surrounded by smooth plains and intermediate plains units.

Interpretation: Crater materials that are excavated pre-smooth plains target material. This target material was probably what is observable today as icp^5.

3.2.5. Smooth Crater Floor (cfs)

Smooth, sparsely cratered material confined to crater floors (Wright et al., 2019).

cfs^6—Occurs within the peak ring of Rachmaninoff, where it contains numerous grabens, and also within the faculae between Rachmaninoff's peak ring and crater rim. It also occurs on the floors of irregular pits in the centers of Nathair Facula and Neidr Facula, as well as on the floors of craters that are embayed by sp^6, some of which are superposed by Nathair Facula.

Interpretation: We interpret the cfs^6 inside Rachmaninoff's peak ring to be effusive volcanic deposits in agreement with previous interpretations (Prockter et al., 2010; Wright, Byrne, & Rothery, 2021). This interpretation is based on SU6 being the most widespread SU of the geomorphically similar smooth plains, which have been shown to be mostly volcanic in origin (Denevi et al., 2013). Furthermore, the formation of grabens within Rachmaninoff was most successfully modeled within a thick, cooling lava layer (Blair et al., 2013). Similarly, we interpret the cfs^6 that occurs in association with Suge Facula and other minor faculae in the annulus between Rachmaninoff's peak ring and crater rim to be distal volcanic flows sourced from within the peak ring, again in agreement with previous interpretations (Wright, Byrne, & Rothery, 2021). We interpret that the cfs^6 found in the irregular pits within faculae are explosive volcanic deposits that fell back into and mantled the explosively excavated volcanic craters (Pegg, Rothery, Balme, & Conway, 2021). Other crater floors bearing cfs^6 but without superposing faculae probably acquired their spectral signature by impact gardening from adjacent sp^6.

cfs^8—Mostly occurs on Rachmaninoff's floor in the annulus between the southern gap in the peak ring and the crater rim, with additional minor exposures within the peak ring. Outside the peak ring, it coincides with weaker faculae within Rachmaninoff, and around the edges of stronger faculae, such as Suge Facula (cfs^6), and other SU6-bearing geostratigraphic units, which might suggest the superposition of cfs^8 by cfs^6. It also occurs on the floors of two craters superposing Rachmaninoff's impact ejecta northwest of the crater's rim.

Interpretation: We interpret the cfs^8 on the floors of craters superposing Rachmaninoff's ejecta, which itself bears SU8, as impact melt formed from the same material as Rachmaninoff's impact ejecta.

A confident interpretation of the cfs^8 within Rachmaninoff is more difficult. It is possible that cfs^8 on Rachmaninoff's floor is also impact melt made from an originally SU8-bearing target material, such as icp^8 exposed beyond Rachmaninoff's northeastern ejecta. This interpretation is consistent with cfs^8 being a minor component of Rachmaninoff's crater floor within the peak ring from where volcanic infilling seems to have emanated, with cfs^8 being more extensive beyond the southern gap in the peak ring where volcanic flows are suggested to have terminated (Wright, Byrne, & Rothery, 2021).

Alternatively, cfs^8 could be volcanic plains, because of their spatial association with cfs^6, which we confidently interpret as volcanic in origin. However, it is not clear why the volcanics within Rachmaninoff might have spatially variable spectra because of compositional variation. It is possible that heterogeneities in the melt source region, a complex magma plumbing system under Rachmaninoff, or melt composition evolution associated with a prolonged eruptive history might have developed spectrally distinct lavas, but supporting evidence for these hypotheses, such as observable source vents associated with the different cfs materials or a clear stratigraphic relationship between cfs^8 and cfs^6 materials, is lacking. Instead, the spectral variation of lavas with a homogeneous erupted composition might be the result of a secondary effect.

Without evidence for long-lived volcanism within Rachmaninoff, it is difficult to explain how its spectrally diverse candidate volcanic units could have arisen. It is possible that cfs^8 and cfs^6 represent volcanic plains of the same composition and age but with different physical properties (such as grain size) such that their responses to space weathering (darkening and reddening) caused them to diverge spectrally. cfs^8 has a lower reflectance at all MDIS wavelengths than cfs^6 but the greatest difference in reflectance between cfs^8 and cfs^6 is at redder wavelengths. Perhaps space weathering has preferentially darkened cfs^8 but left it relatively unreddened compared with surrounding cfs^6 (Lucey & Riner, 2011). However, there is no supporting evidence for significant grain size variation within Rachmaninoff, or any other volcanic plains on Mercury yet. This hypothesis can be tested by maps of grain size estimated from thermal inertia measurements by the Mercury Radiometer and Thermal Infrared Spectrometer (MERTIS: Hiesinger et al., 2020) instrument on BepiColombo.

Looking at the spectral and geostratigraphic maps of Rachmaninoff, it is clear that there is a high spatial concentration of different SUs associated with different morphostratigraphic units distributed at different elevations. An alternative explanation for the spectral diversity in Rachmaninoff is that some of the SUs present within Rachmaninoff result from mixing of endmember SUs. Physical mixing could take place by a combination of factors. cfs^8 within Rachmaninoff could represent a mixture of cfs^6, distributed by effusive and explosive volcanism, and darker, bluer material within the peak ring and crater rim (e.g., $c_4{}^4$), possibly distributed by mass wasting and impact gardening. The observed spatial arrangement of geostratigraphic units within Rachmaninoff is difficult to explain solely with lateral mixing, but vertical mixing by impact cratering depositing originally underlying low-reflectance material on top of cfs^6 could generate cfs^8.

Alternatively, spectral variability of lavas of Rachmaninoff's floor might arise from spatially heterogeneous reactions with substrate volatiles. It has been observed that sulfurous sublimate deposits around millimeter-scale cracks in cooling terrestrial lavas can locally alter the reflectance spectra, with a noted effect being an increase in reflectance at VNIR (Rothery et al., 1996). Mercury's surface is enriched in sulfur compared with Earth (Nittler et al., 2011) and so it is conceivable that similar sublimate deposition might have been an important process on Mercury, although the exact speciation of any sublimates would most likely differ. Pitted ground on Mercury is postulated to form when lavas flowed over volatile-rich substrates, causing pits to form in the lava surfaces (Thomas et al., 2014; Wright, Byrne, & Rothery, 2021). It is possible that there are more lava-substrate interactions on Mercury that have a spectral signature with no presently observable morphological expression.

Because of the contrasting SUs in close spatial association with each other within Rachmaninoff, we believe it is probable that the cfs^8 present there either formed as: (a) impact melt of an SU8-bearing target material, similar to the formation of most of Rachmaninoff's ejecta as $c_4{}^8$; (b) the product of physical mixing of cfs^6 volcanic plains with nearby, spectrally darker and bluer materials from the crater rim and peak ring, or; (c) the outcome of heterogeneous lava-substrate interactions. Of these hypotheses, we think (b) most fits the available data, but (c) remains an intriguing possibility to be investigated by BepiColombo.

cfs^5—Occurs within Rachmaninoff's peak ring where it hosts some grabens. Also occurs on the smooth floors of impact craters superposed by Rachmaninoff's northeastern impact ejecta, and one impact crater in the northwest corner of the mapping area.

Interpretation: As with the cfs^8 within Rachmaninoff's peak ring, the cfs^5 is located among several other geostratigraphic units. We interpret cfs^5 within Rachmaninoff's peak ring as effusive volcanic post-impact infill that has had its original SU (probably SU6) mixed with surrounding darker materials.

It seems unlikely that the cfs^5 in the craters northeast of Rachmaninoff and in the northwest of the mapping area were formed by spectral mixing for two reasons: (a) the three craters are proximal to sp^6 but to no potentially darkening geostratigraphic units, and (b) the two craters northeast of Rachmaninoff have floors with strikingly sharp spectral contacts that coincide with their morphostratigraphic contacts at their crater walls. Instead, we interpret that these three craters have original impact melt on their floors exhibiting primary SU5. This could have formed by the impact occurring on a mixed target, with the melting process mixing the target compositions together.

cfs^4—Occurs as a single contiguous exposure in the northeast of the annulus between Rachmaninoff's peak ring and crater rim. SU4-bearing geostratigraphic units are coincident with Mercury's low-reflectance material (Denevi et al., 2009; Klima et al., 2018).

Interpretation: We interpret cfs^4 as low-reflectance material from the target that has been redeposited as impact melt. SU4 is an endmember SU throughout H05 (Zambon et al., 2022), so it cannot have been formed by mixing of other SUs.

3.2.6. Hummocky Crater Floor (cfh)

Rough or cratered material confined within crater floors (Wright et al., 2019).

cfh^6—Occurs mostly on the floors of irregular pits and impact craters that host faculae. It also occurs on the floor of a degraded impact crater that has been embayed by sp^6 in the north of the mapping area.

Interpretation: Where this unit occurs within an irregular pit, we interpret this as the most recent eruption site, which is unmantled by pyroclasts from earlier eruptions. Elsewhere, we interpret this unit as a degraded crater floor texture that has had its original spectral signature overprinted by SU6 as a result of superposition by a facula or physical mixing with adjacent sp^6, most likely by impact gardening.

cfh^8—Occurs exclusively within Rachmaninoff adjacent to its peak ring.

Interpretation: Rachmaninoff crater floor that has exposed SU8-bearing target materials (icp^8?), similar to $c_4{}^8$ in Rachmaninoff's impact ejecta.

cfh^{10}—Occurs exclusively within the annulus between Rachmaninoff's peak ring and crater rim. It has a more muted texture than cfh geostratigraphic units within Rachmaninoff.

Interpretation: Exposed original Rachmaninoff crater floor texture that, probably due to embayment, has incorporated a quantity of the crater's impact melt.

cfh^4—Occurs exclusively within the annulus between Rachmaninoff's peak ring and crater rim. Most of this unit is situated adjacent to the peak ring.

Interpretation: Exposed original Rachmaninoff crater floor texture that has largely escaped incorporation of impact melt but instead incorporates low-reflectance material excavated from the deepest depths sampled by this crater.

3.3. Merged Geostratigraphic Units

When we initially completed the process of fusing the morphostratigraphic units and SUs within Rachmaninoff one of the geostratigraphic units formed was cfs^{10}: a smooth plains unit confined to some parts of Rachmaninoff's floor with SU10. Based on our interpretation that sp^{10} outside the crater rim is Rachmaninoff impact melt, we also interpreted cfs^{10} as the same material within the crater. As a result, we changed all would-be instances of cfs^{10} to sp^{10} to make this interpretation clear in the map.

Table 1
Summary of the Geostratigraphic Units in the Mapping Area

Geostratigraphic unit	Description	Interpretation
Plains units		
sp^{6}	Smooth plains with high reflectance and steep spectral slope, found in Borealis Planitia and west and southeast of Nathair Facula	Effusive volcanic plains formed toward the end of Mercury's large-volume eruptive history
sp^{8}	Small patches of smooth plains with intermediate reflectance and spectral slope, perched in Rachmaninoff's proximal impact ejecta	Ponded Rachmaninoff impact melt composed of SU8-bearing (icp^{8}?) target material
sp^{5}	Smooth plains with intermediate reflectance and spectral slope, southernmost extent of Borealis Planitia in contact with low-reflectance crater materials	Thin effusive volcanic plains whose original SU6 spectral signature has been mixed with SU5-bearing craters and plains (icp^{5}?) materials nearby
sp^{10}	Smooth plains with low reflectance and shallow spectral slope, found on Rachmaninoff's northern crater floor and perched in its proximal impact ejecta in the northwest, southwest, and southeast interspersed with c_{4}^{10}	Ponded Rachmaninoff impact melt formed by melting low-reflectance material
ip^{6}	Plains with texture intermediate between smooth and intercrater plains with high reflectance and steep spectral slope, single exposure in northwest adjacent to a crater containing a minor facula	Effusive volcanic plains (sp^{6}-type?) that have partially inundated older intercrater plains—spectral signature comes from mantling explosive volcanic deposit
ip^{8}	Plains with texture intermediate between smooth and intercrater plains with intermediate reflectance and spectral slope (SU8), beyond Rachmaninoff's northwestern ejecta	Effusive volcanic materials that have partially inundated older intercrater plains—spectral signature (SU8) comes from mixing with surrounding units
ip^{5}	Plains with texture intermediate between smooth and intercrater plains with intermediate reflectance and spectral slope (SU5), beyond Rachmaninoff's northwestern ejecta	Effusive volcanic materials that have partially inundated darker underlying intercrater plains—spectral signature (SU5) comes from mixing with surrounding units
icp^{6}	Heavily cratered plains with high reflectance and steep spectral slope, in contact with sp^{6} and/or with superposing faculae in north of mapping area	Old effusive volcanic plains incorporating impact ejecta—present spectral signature comes from mixing with surrounding units and superposing explosive volcanic deposits
icp^{8}	Heavily cratered plains with intermediate reflectance (higher than SU5) and spectral slope, found northwest of Rachmaninoff's c_{4}^{8} ejecta	Old effusive volcanic plains, probably incorporating ancient impact ejecta—similar to icp^{5} but with SU8 instead
icp^{5}	Heavily cratered plains with intermediate reflectance (lower than SU8) and spectral slope, found northwest of Rachmaninoff's ejecta	Old effusive volcanic plains, probably incorporating ancient impact ejecta—similar to icp^{8} but with SU5 instead
Crater materials		
c_{4}^{6}	Rachmaninoff materials with high reflectance and steep spectral slope, either:	Rachmaninoff materials, whose spectral signature has been altered volcanism, interpreted as:
	1. Extensive, feather-like textured materials distal to Rachmaninoff, or;	1. Thin, distal Rachmaninoff ejecta superposing sp^{6}
	2. Areally-limited rugged materials associated with faculae within Rachmaninoff	2. Rachmaninoff peak ring and crater rim elements mantled by subsequent explosive volcanic deposits
c_{4}^{8}	Well-preserved crater materials with intermediate reflectance and spectral slope, either:	Crater excavated materials, exhibiting the target material (icp^{8}?) spectral signature, either:
	1. Extensive, feather-liked textured materials surrounding Rachmaninoff its large superposing craters, or;	1. Impact ejecta of Rachmaninoff and its large superposing craters, or;
	2. Rugged material forming the crater walls and central uplift of Rachmaninoff and its large superposing craters	2. The same material uplifted in the crater walls and central uplift of Rachmaninoff and its large superposing craters
c_{4}^{5}	Areally minor materials with a feather-like texture and intermediate reflectance and spectral slope, found around Rachmaninoff and one of its superposing craters	Impact ejecta exhibiting the spectral signature of the target material (icp^{5}?)
c_{4}^{10}	Rachmaninoff materials with low reflectance and shallow spectral slope, either:	Excavated materials that incorporate impact-melted low-reflectance material, either:
	1. Proximal, rim-exterior material with a feather-like texture, in contact with sp^{10}	1. Impact ejecta associated with crater exterior impact melt ponds, or;
	2. Rugged material in Rachmaninoff's walls and floor, in contact with sp^{10}	2. Exposed wall and floor materials draped/embayed by impact melt

Table 1
Continued

Geostratigraphic unit	Description	Interpretation
c_4^4	Rachmaninoff materials with very low reflectance and shallow spectral slope, either:	Low-reflectance material excavated by Rachmaninoff from a deeper substratum than c_4^8
	1. Mountainous peak ring elements (major component), or;	
	2. Hummocky floor, wall, and proximal ejecta (minor component)	
c_3^6	Various moderately degraded crater materials with high reflectance and steep spectral slope in contact with sp^6 and/or superposed by faculae	Excavated materials of unknown original spectral signature—present spectral signature is either that of superposing pyroclastic deposit or result of mixing with surrounding volcanic plains
c_3^8	Moderately degraded crater ejecta with intermediate reflectance (higher than SU5) and spectral slope	Old effusive volcanic plains (icp^8?) redeposited as impact ejecta
c_3^5	Moderately degraded crater materials with intermediate reflectance (lower than SU8) and spectral slope	Old effusive volcanic plains (icp^5?) redeposited as impact ejecta
c_2^6	Various very degraded crater materials with high reflectance and steep spectral slope in contact with sp^6 and superposed by Nathair Facula	Various impact-excavated materials that have had their original spectral unit overprinted by SU6 because of mixing with embaying sp^6 or superposition of distal Nathair Facula pyroclasts
c_2^8	Areally minor, very degraded crater materials with intermediate reflectance and spectral slope found in a single crater in the northwest of the mapping area	Old effusive volcanic plains (icp^8?) excavated and deposited as impact ejecta
c_1^6	Various extremely degraded crater materials with high reflectance and spectral slope in contact with sp^6 and superposed by Nathair Facula	Various impact-excavated materials that have had their original spectral unit overprinted by SU6 because of mixing with embaying sp^6 or superposition of distal Nathair Facula pyroclasts
c_1^8	Extremely degraded crater exterior materials with intermediate reflectance and spectral slope, found in single crater in northwest of mapping area	Old effusive volcanic plains (icp^8?) excavated and deposited as impact ejecta
c_1^5	Various extremely degraded crater materials with intermediate reflectance and spectral slope, found in crater in northwest of mapping area	Old effusive volcanic plains (icp^5?) excavated and uplifted by impacts as ejecta and crater walls
cfs^6	Smooth materials with high reflectance and steep spectral slope, confined to crater floors, either:	Either:
	1. Within Rachmaninoff's peak ring, or;	1. Post-impact effusive volcanic plains akin to sp^6, or;
	2. Within irregular depressions within faculae, or;	2. Smooth mantling fallback pyroclastic deposits on floors of explosively excavated volcanic craters, or;
	3. Within degraded impact craters in contact with sp^6	3. Impact melt in craters that has secondarily acquired an SU6 spectral signature by lateral mixing
cfs^8	Smooth materials with intermediate reflectance and spectral slope, confined to crater floors, either:	Either:
	1. In large impact craters superposing Rachmaninoff ejecta, or;	1. Re-melted Rachmaninoff c_4^8 impact ejecta, or;
	2. In Rachmaninoff	2. SU8 Rachmaninoff impact melt or post-impact volcanic plains (SU6) with secondary SU8 signature acquired by mixing with nearby darker materials or interaction with volatile-rich substrate
cfs^5	Smooth materials with intermediate reflectance and spectral slope, confined to crater floors, either:	Either:
	1. In Rachmaninoff, or;	1. Post-impact volcanic plains (SU6) with secondary SU5 signature acquired by lateral mixing with nearby darker materials or interaction with volatile-rich substrate, or;
	2. In various degraded craters	2. Impact melt of old volcanic effusive volcanic plains (icp^5)
cfs^4	Smooth materials with very low reflectance and shallow spectral slope within Rachmaninoff	Impact-melted low-reflectance material

Table 1
Continued

Geostratigraphic unit	Description	Interpretation
cfh^6	High reflectance and steep spectral slope hummocky material confined to crater floors, either:	Either:
	1. Irregular depressions hosted within faculae, or;	1. Youngest eruption site within explosively excavated volcanic crater mantled by fallback SU6 pyroclasts, or;
	2. One impact crater in contact with sp^6 in the north of the mapping area	2. Original crater floor without impact melt cover with secondary SU6 signature acquired by lateral mixing with nearby sp^6
cfh^8	Intermediate reflectance and spectral slope hummocky materials adjacent to Rachmaninoff's peak ring	SU8-bearing target material (icp^8?) exposed in Rachmaninoff's crater floor
cfh^{10}	Low reflectance and shallow spectral slope hummocky material in the annulus between Rachmaninoff's peak ring and crater rim	Target material exposed in the crater floor that has been embayed, and possibly draped by, Rachmaninoff impact melt
cfh^4	Very low reflectance and shallow spectral slope hummocky material in the annulus between Rachmaninoff's peak ring and crater rim, mostly adjacent to the peak ring	Exposed crater floor with excavated low-reflectance material

4. Discussion

4.1. Geological History of the Rachmaninoff Study Region

The oldest geological events in the study region for which there is any evidence are the formations of the probable impact basins b72 and b96 indicated in the global digital elevation model of Mercury (Figure 6; Orgel et al., 2020). The basement rock unit that these impacts occurred in is not visible in the study region, but it is probable that is either an ancient volcanic crust, or primary flotation crust incorporating low-reflectance material (Klima et al., 2018; Vander Kaaden & McCubbin, 2015). This hypothesis is supported by low-reflectance material present within Rachmaninoff, whose crater interior includes the lowest surface elevation on Mercury (Becker et al., 2016) and under which is some of the planet's thinnest crust (Beuthe et al., 2020), which means Rachmaninoff has excavated into the lowermost parts of Mercury's crustal stratigraphy.

Irrespective of the origin of the basement and the formation of the probable impact basins, the first events for which there is geological evidence recorded in the map are the formations of the c_1 craters. c_1 craters are embayed by all three plains types. Embayment of c_1 craters by intercrater plains indicates that intercrater plains emplacement, probably mostly by effusive volcanism (Whitten et al., 2014), outlasted the formation of these craters. c_1 crater materials and intercrater plains characteristically exhibit SU8 or SU5, except where they have obviously acquired an SU6 signature from a nearby, younger volcanic source. Therefore we interpret SU8 and SU5 to signify optically mature regolith formed from Mercury's ancient composition material.

c_2 craters are not so strongly embayed by intercrater plains as they are by intermediate and smooth plains. We interpret that c_2 craters formed within a span of geological time overlapping intercrater plains emplacement, and that intermediate and smooth plains emplacement postdate c_2 craters and intercrater plains. c_3 craters superpose c_2 craters but are embayed by intermediate and smooth plains in some places, so we interpret that c_3 craters formed within a span of geological time overlapping emplacement of both these plains types.

The smooth plains outside Rachmaninoff, including the southernmost extent of Borealis Planitia, were deposited as large-volume volcanic flows toward the end of effusive eruptive activity on Mercury (Byrne et al., 2016). They characteristically exhibit SU6, except close to their contacts with other units with different spectral signatures. SU6 is higher reflectance and redder than SU8 and SU5, both characteristically exhibited by intercrater plains. This is consistent with suggestions that Mercury's magma composition evolved from lower and bluer (intercrater plains) to higher and redder (smooth plains) reflectances in geological time (Namur & Charlier, 2017). Intermediate plains occur in contact with smooth plains and exhibit the same stratigraphic relationships with crater materials as smooth plains. Thus, we interpret intermediate plains as lava of the same age and composition as sp^6 that has incompletely inundated the underlying material, in agreement with previous work (Wright, Byrne, &

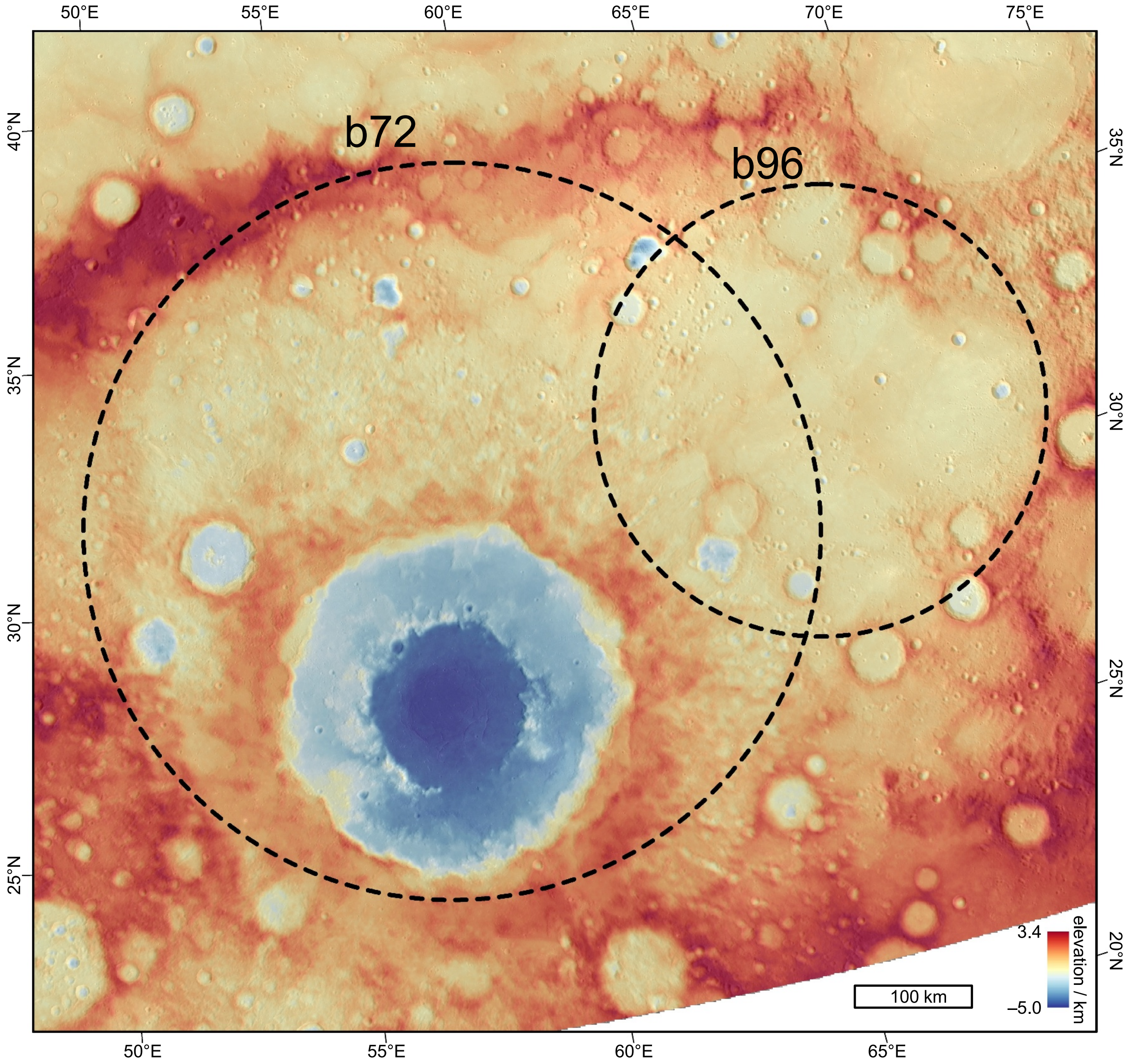

Figure 6. Topography of the study area highlighting probable ancient basins that predate Rachmaninoff (Orgel et al., 2020). 222 m/pixel digital elevation model (Stark et al., 2017) in the default Lambert conformal conic projection of H05 (Wright et al., 2019).

Rothery, 2021). The implied low thicknesses of intermediate plains exposures are consistent with their more spatially variable spectral behavior than the volcanic smooth plains units.

Rachmaninoff is the stratigraphically lowest c_4 crater, and its distal ejecta ($c_4{}^6$, $c_4{}^8$, and $c_4{}^5$) superpose the extensive smooth plains between itself and Nathair Facula. We interpret that these smooth plains and those of Borealis Planitia formed within the same span of geological time, and thus interpret that Rachmaninoff postdates the formation of both. Several geostratigraphic crater materials associated with Rachmaninoff were emplaced during the impact process, including: sp^8 and sp^{10}, which we interpret as Rachmaninoff impact melt, and; $c_4{}^8$, $c_4{}^5$, $c_4{}^4$, cfh^8, cfh^{10}, and cfh^4, which we interpret as various Rachmaninoff excavated materials. Other Rachmaninoff-associated materials necessarily postdate the impact by an uncertain amount of time (Chapman et al., 2012; Marchi et al., 2011), including cfs^6, which we interpret as post-impact effusive volcanic infill of the crater floor. The fact that Rachmaninoff's post-impact volcanic infill exhibits SU6 indicates that it is probably very similar in composition to the exterior sp^6 plains of Borealis Planitia. This suggests that insufficient time passed between the cessation of large-volume effusive volcanic activity of Mercury, the Rachmaninoff impact, and subsequent volcanic infilling for the VNIR spectrum of Mercury's erupted lavas to change detectably. $c_4{}^8$ is the most abundant c_4 geostratigraphic unit, which is consistent with these craters having exhumed material similar material to older craters and enough time has passed for space weathering to alter the spectra in the same way.

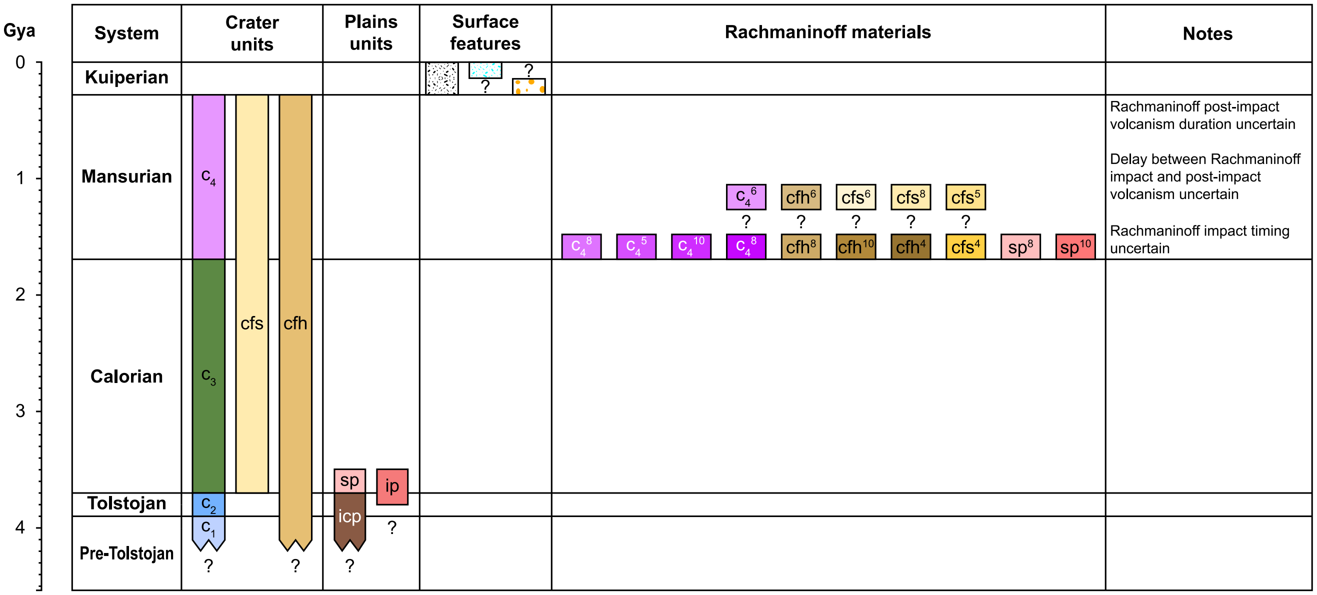

Figure 7. Correlation of geostratigraphic units. Most geostratigraphic units are regrouped back into their morphostratigraphic units on the left. The geostratigraphic units of Rachmaninoff are separated on the right, showing syn- and post-impact units. Estimates of the absolute model ages indicated by the scale on the left are taken from the following literature sources: the bases of the Kuiperian and Mansurian systems (Banks et al., 2017); the bases of the Calorian and Tolstojan systems (Ernst et al., 2017); smooth plains formation (Byrne et al., 2016; Ostrach et al., 2015; Wright, Byrne, & Rothery, 2021), and; intercrater plains formation (Marchi et al., 2013; Whitten et al., 2014).

The uppermost materials in the stratigraphy of the study region are the faculae (including Nathair Facula), hollows, and distal crater rays from the Hokusai impact crater that cross-cut all other materials they are in contact with. Nathair Facula has a unique SU, SU7, which has a redder spectral slope and higher reflectance at all VNIR wavelengths than SU6, which is typical of other faculae and volcanic smooth plains in the study area. This unique spectral response could indicate Nathair Facula is much younger than the rest of the study area, consistent with its position toward the top of the stratigraphy, such that it has undergone less darkening by space weathering than the other faculae. Alternatively, Nathair Facula might have been formed by an explosive eruption that, driven by a high volatile content, fragmented the erupted material to atypically small grain sizes (Kerber et al., 2011). To test these hypotheses, Nathair Facula will be an important target for BepiColombo (Rothery et al., 2020).

Based on these interpretations, we are able to propose a more detailed correlation of map units for the Rachmaninoff study region (Figure 7) than in the morphostratigraphic map of the whole Hokusai quadrangle (Wright et al., 2019). Geomorphic observations remain the primary evidence we used in determining a unit's place in the stratigraphy, as some geostratigraphic units appear to have gained their spectral signatures after their original formation (e.g., $c_4{}^6$, $c_3{}^6$, $c_2{}^6$, $c_1{}^6$). Furthermore, we have created a new indicative geological cross section of the area (see map sheet in Supporting Information S2).

We hypothesize that many geostratigraphic units have acquired their spectral signatures by mixing of their original signature horizontally with surrounding materials and vertically with underlying materials. We favor this kind of interpretation for areally-restricted geostratigraphic units, such as sp^5, found along the boundaries between other major geostratigraphic units with characteristic and contrasting spectral signatures. We leave testing of these interpretations, perhaps by targeted spectral analysis, to a future work.

4.2. Utility of Data Fusion

As shown in the previous section, our data fusion technique has enriched the geological history of the study region compared with what was possible relying on morphostratigaphic units alone (Wright et al., 2019). By combining morphostratigraphic and spectral information we have confidently been able to distinguish Rachmaninoff impact melt ponds (sp^{10}) from other smooth plains, which Wright et al. (2019) could not do. Furthermore, we find that much of Rachmaninoff's textured ejecta in the intervening space between its perched smooth plains patches is the $c_4{}^{10}$ unit. By looking at the relationship between morphostratigraphic units and SUs, we have hypothesized that

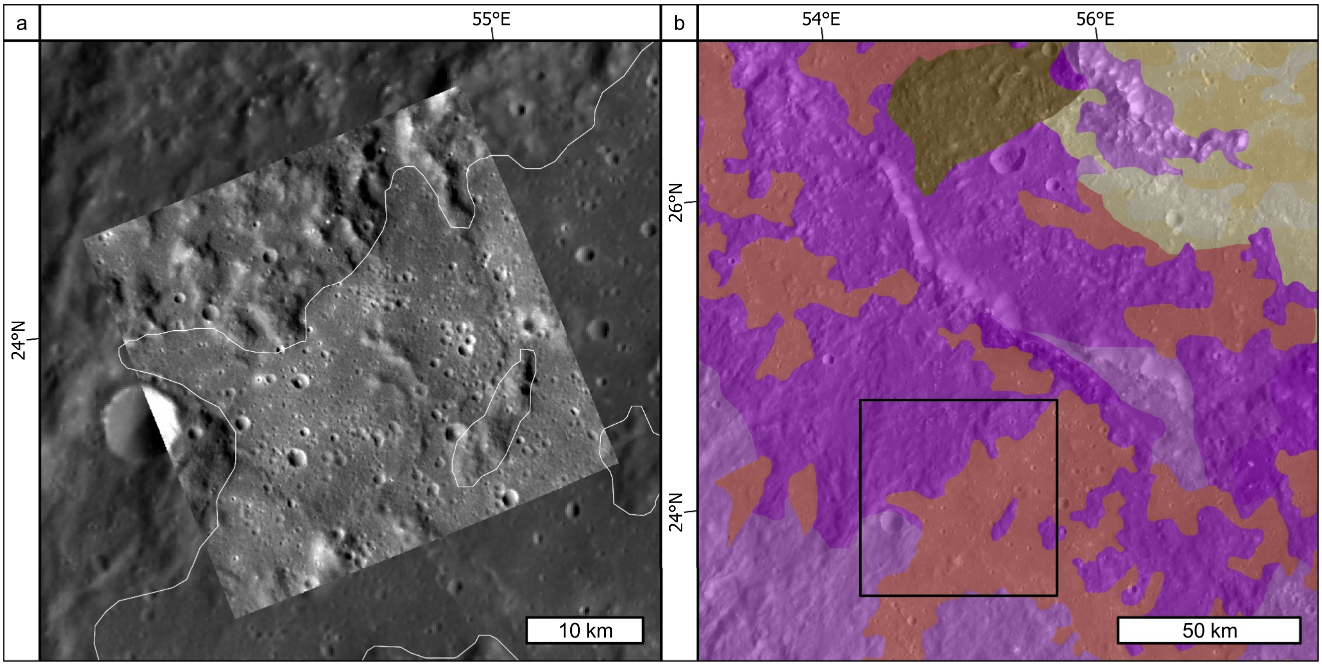

Figure 8. Relationship between SU10 and Rachmaninoff's impact ejecta and melt. (a) Wright, Rothery, et al. (2021) geomorphic contacts (white lines) proximal to Rachmaninoff's crater rim between smooth plains and textured ejecta. In the upper left, discontinuous smooth plains deposits can be seen in a region mapped as textured ejecta. MDIS NAC image EN1004045212M (35 m/pixel) overlain on the 166 m/pixel monochrome mosaic. (b) Geostratigraphic map of southwest Rachmaninoff overlain on the 166 m/pixel monochrome mosaic with the extent of (a) shown by the black box.

Rachmaninoff's impact melt is incorporated into some of its textured ejecta where it has not been able to collect in pools. This is consistent with c_4^{10} being found north of the crater rim, in the probable uprange direction, with only a single mapped patch of sp^{10}: the reduced volume of impact melt deposited north of the crater rim was unable to pond efficiently and left a mostly spectral, rather than geomorphic, signature. To test this hypothesis we examined 30 m/pixel or better MDIS NAC images of Rachmaninoff's c_4^{10} impact ejecta to find local geomorphic evidence of impact melt (e.g., flows; Leight & Ostrach, 2018). Although we found no melt flows within the ejecta such as those seen on the Moon (e.g., Bray et al., 2018) and elsewhere on Mercury (Leight & Ostrach, 2018), we did find more smooth plains superimposed on the crater ejecta that could not be mapped by Wright et al. (2019) because of their mapping scale (Figure 8).

More powerfully, by combining morphostratigraphic units and SUs we been able to subdivide smooth materials in contact with each other on a quantitative basis, allowing us to distinguish between Rachmaninoff's interior impact melt (sp^{10}) and subsequent volcanic plains (cfs^6). The spectrally-defined contact between sp^{10} and cfs^6 coincides with the northern boundary of Suge Facula, which corroborates the hypothesis of Wright, Byrne, and Rothery (2021) that Suge Facula preserves a pitted ground texture (Jozwiak et al., 2018; Thomas et al., 2014) because lavas emanating from the center of Rachmaninoff terminated here and did not sufficiently bury the volatile-bearing substrate. This also supports the hypothesis that spectral variation within the center of Rachmaninoff might be the result of variable lava-substrate interactions, but while a spectral signature is preserved the lavas in the center of the crater are too thick for the pitted ground texture to be preserved (Wright, Byrne, & Rothery, 2021).

There is a network of grabens within Rachmaninoff's peak ring that Blair et al. (2013), based on modeling, proposed to have formed because of thermal contraction of a thick volcanic unit. While many of the aspects of the observed graben network are reproduced by their modeling, the models consistently predicted a graben network extending over the center of the basin, rather than the observed annulus of grabens around the center. Blair et al. (2013) observed that the innermost grabens in the annulus are more topographically muted than those more outward from the center of the basin and suggest that this could be a result of partial inundation of these grabens by late-stage lava flows emanating from the center of the basin, where grabens were supposedly completely obscured. This hypothesis would be corroborated by the observation of a distinct geostratigraphic unit within the graben annulus indicative of lava plains spectrally, and therefore plausibly temporally, distinct from those elsewhere in Rachmaninoff. However, we find that the pattern of geostratigraphic units within the peak ring of Rachmaninoff (an assortment of cfs^5, cfs^6, and cfs^8) shows no clear spatial relationship with the graben network (Figure 2d). Therefore, all we can conclude from our observations is that if multiple generations of effusions did occur within Rachmaninoff, then they appear not to have had different primary compositions (but heterogeneous substrate interactions might have produced some spectral variability) and probably occurred within a span of geological time that was short when compared with the difference in formation times of the volcanic plains within other impact basins on Mercury, such as Rembrandt (Semenzato et al., 2020).

4.3. Previous Integrations of Morphostratigraphic and Spectral Units

Our method is similar to that of Yingst et al. (2023), who also made morphostratigraphic and spectral maps of Vesta before merging them. Our methods were derived independently and have some important differences. Yingst et al. (2023) did not quantitatively define their SUs of Vesta as Zambon et al. (2022) did for H05 on Mercury. Yingst et al. (2023) defined a decision tree for determining whether geomorphological or spectral data should be used to define the position of a geological unit boundary where these data disagree and the position is ambiguous. In our map, as described earlier, where morphostratigraphic and spectral contacts closely coincide, we always retain the morphostratigraphic contact because these have been created using higher spatial resolution data sets than the spectral contacts. Yingst et al. (2023) found that Vesta's geomorphology is blurred because of impact cratering. We found that Mercury preserves sharp morphostratigraphic contacts, particularly at the boundaries of the extensive smooth plains throughout our study area: a unit type not found on Vesta (Yingst et al., 2023). Our method is applicable to regions of planetary surfaces where pre-existing morphostratigraphic and spectral maps are already available. In the future, when confronted with a planetary mapping area that warrants the fusion of morphostratigraphic and SUs, a mapper could choose to follow our method, that of Yingst et al. (2023), or another method. Mappers should always follow the method that will best serve their science goals.

A similar method to the one presented in this work has already been employed to useful effect by Canale et al. (2024). They first mapped morphostratigraphic and SUs (manually) of Sibelius crater, Mercury, based on MESSENGER monochrome and enhanced color MDIS basemaps, respectively. They created their hybrid map by merging these two input products. The innovation of the present work is that the input SUs were independently and quantitatively defined (Zambon et al., 2022), which should increase the reproducibility of the final geostratigraphic map.

Semenzato et al. (2020) used a different approach. They made two maps of Rembrandt basin: the first is a conventional morphostratigraphic map based on monochrome basemaps in keeping with the MESSENGER-era quadrangle geological maps of Mercury (Galluzzi et al., 2016, 2021; Giacomini et al., 2022; Guzzetta et al., 2017; Malliband et al., 2022; Man et al., 2023; Mancinelli et al., 2016; Pegg, Rothery, Balme, et al., 2021; Wright et al., 2019), and the second is based on false color basemaps, where contacts are between units separated on the basis of their colors, stratigraphic positions, and crater retention ages. As with the present work, Semenzato et al. (2020) argue that color variations on Mercury can mostly be attributed to variations in either composition or space weathering exposure. Thus, where spectral effects of optical maturity can be isolated, surfaces with distinct colors throughout the mapping area can be correlated as rock units of the same composition, similar to geological units on Earth.

Our geostratigraphic map of Rachmaninoff and its surroundings is a similar product to the Semenzato et al. (2020) geostratigraphic map of Rembrandt, with some key differences in their methods of production. Most obviously, while the Rembrandt geostratigraphic map was produced alongside a conventional morphostratigraphic map of the same area, the morphostratigraphic map was not an input, or even a prerequisite, for the geostratigraphic map (Semenzato et al., 2020), unlike in our method shown here. Furthermore, Semenzato et al. (2020) created their map without a predefined spectral map, instead manually assessing the boundaries of color units. In this way, the Semenzato et al. (2020) method can produce geostratigraphic maps potentially much more rapidly than our method shown here because the integration of morphostratigraphic and spectral information is done "in parallel," rather than "in series" as we have done.

Nevertheless, our method has some advantages. Our method can be applied retroactively to existing planetary morphostratigraphic maps where complementary spectral data exist, without having to map new geostratigraphic units from scratch (Giacomini et al., 2021, 2022). Our method incorporates SUs with consistently applied, computationally defined characteristics and extents, rather than human-eye interpretations of color boundaries. Furthermore, since the number of SUs was not arbitrarily set (Zambon et al., 2022), this meant that the necessary and sufficient quantity of SUs to characterize the study area emerged, rather than too few, as might be the case if they were too subtle to be distinguished by the human eye, or too many.

Despite the differences in their methods of production, both the Semenzato et al. (2020) geostratigraphic map and ours reveal similar results. In their morphostratigraphic map, Semenzato et al. (2020) identified a single smooth plains unit within Rembrandt based on the strictly geomorphic definition of this unit. However, they could subdivide the smooth plains within Rembrandt on the basis of color. They interpret these two geostratigraphic units as two different generations of infilling volcanic plains. This hypothesis is supported by indications of resurfacing seen in the crater size frequency distribution of Rembrandt's interior smooth plains (Semenzato et al., 2020). This is a similar result to our subdivision of the smooth crater floor material of Rachmaninoff into probable impact melt and volcanic plains based on their different spectral properties.

We consider the development of spectral integration methods and the creation of our geostratigraphic maps to be important preparation for the upcoming ESA-JAXA BepiColombo mission to Mercury (Benkhoff et al., 2021), whose best science will come from focusing its many instruments on targets with key information, such as Rachmaninoff and its surroundings (Rothery et al., 2020).

4.4. Wider Application of In-Series Geostratigraphic Integration

Now that the data fusion process has been demonstrated to yield useful geological insight that hitherto has been absent from traditional Mercury geological maps, the obvious next step would be to attempt the data fusion over the entirety of H05. This might allow further instances of impact melt and post-impact volcanic plains in contact with each other to be distinguished. Furthermore, it would allow subdivision of Borealis Planitia on quantifiable grounds. This is similar to the problem of Caloris Planitia and the surrounding circum-Caloris plains, which are inseparable on a purely morphostratigraphic basis (Rothery et al., 2017).

Beyond H05, SU analyses comparable to the one used by this study are available for the Shakespeare (H03: Bott et al., 2019) and Kuiper (H06) quadrangles, and the spectral integration process for H06 is underway (Giacomini et al., 2021). We envisage that fusion of morphostratigraphic units and SUs will yield particularly interesting scientific insights in H03, which contains part of the Caloris basin. For example, while several studies have looked at the geomorphology and spectral properties of the smooth plains within and around Caloris (Caminiti et al., 2023; Denevi et al., 2013; Rothery et al., 2017), none has yet looked into the exact relationship between the Caloris morphostratigraphic units and their reflectance spectra. This is important work to be done because Caloris is the largest well-preserved impact basin on Mercury and thus has excavated material from great depth and deposited it over a wide area on the planet's surface, making them amenable to different remote sensing analyses. Elsewhere on Mercury, other large basins, such as Beethoven and Tolstoj, are associated with contrasting morphostratigraphic and SUs, making these important areas for future study. Beyond Mercury, the same retrospective data fusion process shown here has been implemented by Pöhler et al. (2022) combining geomorphic (Ivanov et al., 2018) and spectral (Zambon, Carli, Altieri, et al., 2021) maps of the Apollo basin on the Moon.

Here, we have integrated spectral information with morphostratigraphic units to create geostratigraphic units. Ideally, we would like to integrate compositional data (e.g., from X-ray spectroscopy; Bunce et al., 2020; Nittler et al., 2020, 2023) into the geostratigraphic units. Whether or not this task is possible with MESSENGER data, we leave this for a future work. Another task we leave for future work is testing if spectral characteristics of real rock units can be imitated by physical mixing of two other geostratigraphic units. One way to test this would be to look for mixing trends in spectral indices. Caminiti et al. (2023) have performed a spectral characterization of Mercury Atmospheric and Surface Composition Spectrometer (MASCS: McClintock & Lankton, 2007) spectra of Caloris-associated units, similar to the spectral characterization of H05 units in MDIS data by Zambon et al. (2022). Caminiti et al. (2023) used spectral indices to identify high-reflectance red plains, low-reflectance blue plains, and low-reflectance material within and around the Caloris basin. Atget crater lies on Caloris Planitia, which is a high-reflectance red plain, but Atget has exhumed low-reflectance material on its floor. The Caminiti et al. (2023) spectral indices uncontroversially identify the high-reflectance red plains and low-reflectance material outside and inside the crater, respectively, but they also identify low-reflectance blue plains in Atget's intervening impact ejecta (see their Figure 7). The spectral appearance of low-reflectance blue plains could be mimicked by a mixture of high-reflectance red plains and low-reflectance material, such as might be expected in Atget's impact ejecta. This hypothetical mixing could be detected if the spectral index values for the ejecta lie on a mixing trend continuum between pure high-reflectance red plains and low-reflectance material values. However, Caminiti et al. (2023) found that the low-reflectance blue plains identified in Atget's impact ejecta has spectral index values that appear to plot in a cloud isolated from high-reflectance red plains and low-reflectance material, which suggests real low reflectance blue plains have been exhumed rather than imitated by spectral mixing. It remains to be seen how many of the geostratigraphic units we have identified are the results of mixing of other endmember SUs.

4.5. Geostratigraphic Maps of Mercury With BepiColombo Data Sets

Here we have demonstrated that morphological data can be fused with spectral data with a similar spatial resolution. The upcoming BepiColombo mission will provide new data sets with which to study the Solar System's innermost planet (Benkhoff et al., 2021). The best surface science will come from combining the results of its multiple instruments onboard BepiColombo's Mercury Planetary Orbiter (MPO; Rothery et al., 2020), and geological maps are an obvious way to do this.

The Spectrometer and Imaging for MPO BepiColombo Integrated Observatory SYStem (SIMBIO-SYS; Cremonese et al., 2020) is the scientific imaging camera suite onboard BepiColombo. It consists of three imaging channels: the Stereo imaging Channel (STC); the High Resolution Imaging Channel, and; the VNIR Hyperspectral Imaging (VIHI) channel. In the first 6 months of BepiColombo's nominal mission, STC will provide the monochrome images to make the basemap mosaics (50–120 m/pixel: Cremonese et al., 2020) from which conventional morphostratigraphic maps of Mercury could be made. Like MDIS, STC is a multispectral imager, and it is equipped with four broad-band filters. STC will map Mercury's surface in color (<120 m/pixel) in the second 6 months of BepiColombo's nominal mission (Cremonese et al., 2020). Morphostratigraphic and spectral maps of Mercury made using monochrome and multispectral STC basemaps could be combined following our data fusion method presented in this paper.

However, we expect major advances in incorporating new information to make geostratigraphic maps of Mercury will come from other instruments. VIHI will map Mercury between 400 and 2,000 nm at ~480 m/pixel and the Mercury Radiometer and Thermal Infrared Spectrometer (MERTIS; Hiesinger et al., 2020) will map between 7 and 14 μm at 500 m/pixel. Together these instruments will permit a more comprehensive spectral classification of Mercury, as well as the first mineralogical maps for incorporation into geological maps of the innermost planet. Elemental composition data from Mercury Imaging X-ray Spectrometer (MIXS; Bunce et al., 2020) will be available for data fusion with a more uniform spatial resolution globally because of MPO's relatively circular orbit compared with MESSENGER's. VIHI, MERTIS, and MIXS are all imaging spectrometers, which will ease the data fusion process since spectral properties can be more readily attributed to geological features. With more integrated data sets, the utility of the resultant geostratigraphic maps will be greatly enhanced beyond what we have been able to achieve with our product presented here.

5. Conclusions

We have created an updated map of Rachmaninoff and its surroundings by integrating SUs generated from MDIS data (Zambon et al., 2022) into morphostratigraphic units originally mapped from monochrome MDIS data (Wright et al., 2019). The integrated map communicates more geological information than its constituent morphostratigraphic and SU maps. For example, the integrated map highlights smooth plains of volcanic and impact melt origin in contact with each other that previously were grouped into smooth crater floor material. The integrated map also implies a much wider distribution of Rachmaninoff impact melt beyond the crater rim than is visible in the geomorphology. Rachmaninoff will be an important target for BepiColombo (Benkhoff et al., 2021; Rothery et al., 2020), whose MIXS (Bunce et al., 2020), MERTIS (Hiesinger et al., 2020) and SIMBIO-SYS (Cremonese et al., 2020) instruments can test our hypotheses. In the meantime, the next step will be to create more geostratigraphic maps to see what further insights they can bring.

Data Availability Statement

We used Esri ArcMap 10.6 to digitize the map (ESRI, 2018). We used Esri ArcGIS Pro 3.0 (ESRI, 2022) to make the map figures shown in this work and the Main Map in Supporting Information S2 was assembled in Adobe

Illustrator 28.0 (Adobe Inc, 2023). The MESSENGER MDIS images and mosaics used in this work are publicly available. The 166 m/pixel monochrome mosaic was downloaded from the USGS website https://astrogeology.usgs.gov/search/map/Mercury/Messenger/Global/Mercury_MESSENGER_MDIS_Basemap_BDR_Mosaic_Global_166m and is also described in Hash (2013). MDIS images were downloaded from the NASA Planetary Sata System Geosciences Node Mercury Orbital Data Explorer https://ode.rsl.wustl.edu/mercury/indexDatasets.aspx and are also described in Hash (2008). The morphostratigraphic vector mapping features are available at: https://doi.org/10.5281/zenodo.4773443 (Wright, Rothery, et al., 2021). The spectral unit map is available at: https://doi.org/10.5281/zenodo.4772274 (Zambon, Carli, & Altieri, 2021). The geostratigraphic vector mapping features are available at: https://doi.org/10.5281/zenodo.4773573 (Wright, Zambon, et al., 2021).

Acknowledgments

This work is an output of the PLANMAP project. PLANMAP has received funding from the European Union's Horizon 2020 research and innovation programme under grant agreement no 776276. JW acknowledges support from the European Space Agency (ESA) as an ESA Research Fellow received during the write-up of this work. SJC acknowledges the support of the French Space Agency, CNES for her BepiColombo-related work. The authors are grateful to Peter Fawdon and Elena A. Favaro for discussions on planetary geological mapping during the revision of this manuscript. The authors are grateful to R. Aileen Yingst and one anonymous reviewer, whose comments helped us to improve the clarity of the manuscript. The authors are also grateful to the Editor, David Baratoux, for his comments and editorial handling of the manuscript.

References

Adobe Inc. (2023). Adobe illustrator (28.0) [Software]. Adobe Inc. Retrieved from https://adobe.com/products/illustrator

Banks, M. E., Xiao, Z., Braden, S. E., Barlow, N. G., Chapman, C. R., Fassett, C. I., & Marchi, S. S. (2017). Revised constraints on absolute age limits for Mercury's Kuiperian and Mansurian stratigraphic systems. *Journal of Geophysical Research: Planets*, *122*(5), 1010–1020. https://doi.org/10.1002/2016JE005254

Barraud, O., Besse, S., Doressoundiram, A., Cornet, T., & Muñoz, C. (2021). Spectral investigation of Mercury's pits' surroundings: Constraints on the planet's explosive activity. *Icarus*, *370*, 114652. https://doi.org/10.1016/j.icarus.2021.114652

Becker, K. J., Robinson, M. S., Becker, T. L., Weller, L. A., Edmundson, K. L., Neumann, G. A., et al. (2016). First global digital elevation model of Mercury. In *47th Lunar and Planetary Science Conference, abstract #2959*. Retrieved from https://www.hou.usra.edu/meetings/lpsc2016/pdf/2959.pdf

Benkhoff, J., Murakami, G., Baumjohann, W., Besse, S., Bunce, E., Casale, M., et al. (2021). BepiColombo—Mission overview and science goals. *Space Science Reviews*, *217*(90), 90. https://doi.org/10.1007/s11214-021-00861-4

Besse, S., Doressoundiram, A., Barraud, O., Griton, L., Cornet, T., Muñoz, C., et al. (2020). Spectral properties and physical extent of pyroclastic deposits on Mercury: Variability within selected deposits and implications for explosive volcanism. *Journal of Geophysical Research: Planets*, *125*(5), e2018JE005879. https://doi.org/10.1029/2018JE005879

Beuthe, M., Charlier, B., Namur, O., Rivoldini, A., & Van Hoolst, T. (2020). Mercury's crustal thickness correlates with lateral variations in mantle melt production. *Geophysical Research Letters*, *47*(9), e2020GL087261. https://doi.org/10.1029/2020GL087261

Bibring, J. P., Soufflot, A., Berthé, M., Langevin, Y., Gondet, B., Drossart, P., et al. (2004). OMEGA: Observatoire pour la Minéralogie, l'Eau, les Glaces et l'Activité. In A. Wilson (Ed.), *Mars express: The scientific payload* (Vol. SP-1240). Retrieved from https://adsabs.harvard.edu/full/2004ESASP1240…37B

Blair, D. M., Freed, A. M., Byrne, P. K., Klimczak, C., Prockter, L. M., Ernst, C. M., et al. (2013). The origin of graben and ridges in Rachmaninoff, Raditladi, and Mozart basins, Mercury. *Journal of Geophysical Research: Planets*, *118*(1), 47–58. https://doi.org/10.1029/2012JE004198

Blance, A. J., Rothery, D. A., Balme, M. R., Wright, J., & Galluzzi, V. (2023). Mercury's H11 discovery quadrangle: Mapping progress update. In *54th Lunar and Planetary Science Conference, abstract #2251*. Retrieved from https://www.hou.usra.edu/meetings/lpsc2023/pdf/2251.pdf

Blewett, D. T., Chabot, N. L., Denevi, B. W., Ernst, C. M., Head, J. W., Izenberg, N. R., et al. (2011). Hollows on Mercury: MESSENGER evidence for geologically recent volatile-related activity. *Science*, *333*(6051), 1856–1859. https://doi.org/10.1126/science.1211681

Bott, N., Doressoundiram, A., Zambon, F., Carli, C., Guzzetta, L. G., Perna, D., & Capaccioni, F. (2019). Global spectral properties and lithology of Mercury: The example of the Shakespeare (H-03) quadrangle. *Journal of Geophysical Research: Planets*, *124*(9), 2326–2346. https://doi.org/10.1029/2019JE005932

Bray, V. J., Atwood-Stone, C., Neish, C. D., Artemieva, N. A., McEwen, A. S., & McElwaine, J. N. (2018). Lobate impact melt flows within the extended ejecta blanket of Pierazzo crater. *Icarus*, *301*(February 2018), 26–36. https://doi.org/10.1016/j.icarus.2017.10.002

Bunce, E. J., Martindale, A., Lindsay, S., Muinonen, K., Rothery, D. A., Pearson, J., et al. (2020). The BepiColombo Mercury Imaging X-ray Spectrometer: Science goals, instrument performance and operations. *Space Science Reviews*, *216*(126), 126. https://doi.org/10.1007/s11214-020-00750-2

Buoninfante, S., Galluzzi, V., Ferranti, L., & Milano, M. (2022). Geostructural mapping of the Michelangelo (H-12) quadrangle of Mercury: Relationship between tectonic and crustal structures. In *Europlanet Science Congress 2022, EPSC2022-811*. https://doi.org/10.5194/epsc2022-811

Byrne, P. K., Blewett, D. T., Chabot, N. L., Hauck, S. A., Mazarico, E., Vander Kaaden, K. E., et al. (2021). The case for landed Mercury science. *Experimental Astronomy*, *54*(2–3), 561–573. https://doi.org/10.1007/s10686-021-09788-8

Byrne, P. K., Ostrach, L. R., Fassett, C. I., Chapman, C. R., Denevi, B. W., Evans, A. J., et al. (2016). Widespread effusive volcanism on Mercury likely ended by about 3.5 Ga. *Geophysical Research Letters*, *43*(14), 7408–7416. https://doi.org/10.1002/2016GL069412

Caminiti, E., Doressoundiram, A., Besse, S., & Wright, J. (2023). A spectral study of the Caloris basin on Mercury and the origin of associated volcanic smooth plains. *Journal of Geophysical Research: Planets*, *128*(5), e2022JE007685. https://doi.org/10.1029/2022JE007685

Canale, M., Wright, J., & Rothery, D. A. (2024). A hybrid geological map of Sibelius Crater on Mercury, and its associated ejecta and impact melt deposits. *Geological Society, London, Special Publications*, *541*(1), 2022–2296. https://doi.org/10.1144/SP541-2022-296

Chapman, C. R., Merline, W. J., Marchi, S. S., Prockter, L. M., Fassett, C. I., Head, J. W., et al. (2012). The young inner plains of Mercury's Rachmaninoff basin reconsidered. In *43rd Lunar and Planetary Science Conference, abstract #1607*. Retrieved from https://www.lpi.usra.edu/meetings/lpsc2012/pdf/1607.pdf

Cremonese, G., Capaccioni, F., Capria, M. T., Doressoundiram, A., Palumbo, P., Vincendon, M., et al. (2020). SIMBIO-SYS: Scientific cameras and spectrometer for the BepiColombo mission. *Space Science Reviews*, *216*(75), 75. https://doi.org/10.1007/s11214-020-00704-8

Denevi, B. W., Ernst, C. M., Meyer, H. M., Robinson, M. S., Murchie, S. L., Whitten, J. L., et al. (2013). The distribution and origin of smooth plains on Mercury. *Journal of Geophysical Research: Planets*, *118*(5), 891–907. https://doi.org/10.1002/jgre.20075

Denevi, B. W., Robinson, M. S., Solomon, S. C., Murchie, S. L., Blewett, D. T., Domingue, D. L., et al. (2009). The evolution of Mercury's crust: A global perspective from MESSENGER. *Science*, *324*(5927), 613–618. https://doi.org/10.1126/science.1172226

Domingue, D. L., Chapman, C. R., Killen, R. M., Zurbuchen, T. H., Gilbert, J. A., Sarantos, M., et al. (2014). Mercury's weather-beaten surface: Understanding Mercury in the context of lunar and asteroidal space weathering studies. *Space Science Reviews*, *181*(1–4), 121–214. https://doi.org/10.1007/s11214-014-0039-5

El Yazidi, M., Tognon, G., Galluzzi, V., Giacomini, L., & Massironi, M. (2021). Geology of the Eminescu (H-09) quadrangle: Mapping status. In *Europlanet Science Congress 2021, EPSC2021-682*. https://doi.org/10.5194/epsc2021-682

Ernst, C. M., Chabot, N. L., Klima, R. L., Kubota, S., Rogers, G., Byrne, P. K., et al. (2022). Science goals and mission concept for a landed investigation of Mercury. *The Planetary Science Journal*, *3*(3), 68. https://doi.org/10.3847/PSJ/ac1c0f

Ernst, C. M., Denevi, B. W., & Ostrach, L. R. (2017). Updated absolute age estimates for the Tolstoj and Caloris basins, mercury. In *48th Lunar and Planetary Science Conference, abstract #2934*. Retrieved from https://www.hou.usra.edu/meetings/lpsc2017/pdf/2934.pdf

ESRI. (2018). ArcGIS desktop 10.6 [Software]. Environmental Systems Research Institute. Retrieved from https://www.esri.com/en-us/arcgis/products/arcgis-desktop/resources

ESRI. (2022). ArcGIS Pro 3.0 [Software]. Environmental Systems Research Institute. Retrieved from https://www.esri.com/en-us/arcgis/products/arcgis-pro/resources

Evans, L. G., Peplowski, P. N., Rhodes, E. A., Lawrence, D. J., McCoy, T. J., Nittler, L. R., et al. (2012). Major-element abundances on the surface of Mercury: Results from the MESSENGER gamma-ray spectrometer. *Journal of Geophysical Research*, *117*(E12), E00L07. https://doi.org/10.1029/2012JE004178

Fawdon, P., Skok, J. R., Balme, M. R., Vye-Brown, C. L., Rothery, D. A., & Jordan, C. J. (2015). The geological history of Nili Patera, Mars. *Journal of Geophysical Research: Planets*, *120*(5), 951–977. https://doi.org/10.1002/2015JE004795

Fuechsel, C. F. (2023). map. In *Encyclopedia Britannica (30 Oct. 20)*. Retrieved from https://www.britannica.com/science/map

Galluzzi, V., Di Achille, G., Ferranti, L., Popa, C., & Palumbo, P. (2015). Faulted craters as indicators for thrust motions on Mercury. *Geological Society, London, Special Publication*, *401*(1), 313–325. https://doi.org/10.1144/SP401.17

Galluzzi, V., Guzzetta, L. G., Ferranti, L., Di Achille, G., Rothery, D. A., & Palumbo, P. (2016). Geology of the Victoria quadrangle (H02), Mercury. *Journal of Maps*, *12*(sup1), 227–238. https://doi.org/10.1080/17445647.2016.1193777

Galluzzi, V., Guzzetta, L. G., Mancinelli, P., Giacomini, L., Lewang, A. M., Malliband, C. C., et al. (2018). The making of the 1:3M geological map series of Mercury: Status and updates. In *Mercury: Current and Future Science of the Innermost Planet, abstract #6075*. Retrieved from https://www.hou.usra.edu/meetings/mercury2018/pdf/6075.pdf

Galluzzi, V., Rothery, D. A., Giacomini, L., Guzzetta, L. G., El Yazidi, M., Ferranti, L., et al. (2021). European quadrangle mapping of Mercury: Status report. In *Planetary Geologic Mappers Meeting, abstract #7027*. Retrieved from https://www.hou.usra.edu/meetings/pgm2021/pdf/7027.pdf

Gault, D. E., & Wedekind, J. A. (1978). Experimental studies of oblique impact. In *9th Lunar and Planetary Science Conference* (pp. 3843–3875). Retrieved from https://adsabs.harvard.edu/full/1978LPSC….9.3843G

Giacomini, L., Carli, C., Zambon, F., Galluzzi, V., Ferrari, S., Massironi, M., et al. (2021). Integration between morphological and spectral characteristics for the geological map of Kuiper quadrangle (H06). In *EGU General Assembly 2021, EGU21-15052*. https://doi.org/10.5194/egusphere-egu21-15052

Giacomini, L., Galluzzi, V., Massironi, M., Ferranti, L., & Palumbo, P. (2022). Geology of the Kuiper quadrangle (H06), Mercury. *Journal of Maps*, *18*(2), 246–257. https://doi.org/10.1080/17445647.2022.2035268

Giacomini, L., Guzzetta, L., Galluzzi, V., Ferranti, L., & Palumbo, P. (2023). Preliminary results of Tolstoj quadrangle (H08) geological mapping. In *EGU General Assembly 2023, EGU23-12945*. https://doi.org/10.5194/egusphere-egu23-12945

Goudge, T. A., Head, J. W., Kerber, L., Blewett, D. T., Denevi, B. W., Domingue, D. L., et al. (2014). Global inventory and characterisation of pyroclastic deposits on Mercury: New insights into pyroclastic activity from MESSENGER orbital data. *Journal of Geophysical Research: Planets*, *119*(3), 635–658. https://doi.org/10.1002/2013JE004480

Green, R. O., Pieters, C., Mouroulis, P., Eastwood, M., Boardman, J., Glavich, T., et al. (2011). The Moon Mineralogy Mapper (M3) imaging spectrometer for lunar science: Instrument description, calibration, on-orbit measurements, science data calibration and on-orbit validation. *Journal of Geophysical Research*, *116*, E00G19. https://doi.org/10.1029/2011JE003797

Guzzetta, L. G., Galluzzi, V., Ferranti, L., & Palumbo, P. (2017). Geology of the Shakespeare quadrangle (H03), Mercury. *Journal of Maps*, *13*(2), 227–238. https://doi.org/10.1080/17445647.2017.1290556

Guzzetta, L. G., Lewang, A. M., Mosca, A., Ferranti, L., Hiesinger, H., & Palumbo, P. (2018). Preliminary geologic map of the Beethoven quadrangle (H07), Mercury. In *Congresso SGI-SIMP, 830*. Retrieved from https://www.researchgate.net/publication/332073638_Preliminary_geologic_map_of_the_Beethoven_Quadrangle_H07_Mercury

Hargitai, H., & Naß, A. (2019). Planetary mapping: A historical overview. In H. Hargitai (Ed.), *Planetary cartography and GIS. Lecture notes in geoinformation and cartography* (pp. 27–64). Springer. https://doi.org/10.1007/978-3-319-62849-3_2

Hash, C. (2008). Messenger MDIS experiment (EDR) data E/V/H V1.0 [Dataset]. NASA Planetary Data System. https://doi.org/10.17189/1520380

Hash, C. (2013). Messenger MDIS map projected basemap RDR V1.0 [Dataset]. NASA Planetary Data System. https://doi.org/10.17189/1520406

Hawkins, S. E., Boldt, J. D., Darlington, E. H., Espiritu, R., Gold, R. E., Gotwols, B., et al. (2007). The Mercury dual imaging system on the MESSENGER spacecraft. *Space Science Reviews*, *131*(1–4), 247–338. https://doi.org/10.1007/s11214-007-9266-3

Hiesinger, H., Helbert, J., Alemanno, G., Bauch, K. E., D'Amore, M., Maturilli, A., et al. (2020). Studying the composition and mineralogy of the Hermean surface with the Mercury Radiometer and Thermal Infrared Spectrometer (MERTIS) for the BepiColombo mission: An update. *Space Science Reviews*, *216*(110), 110. https://doi.org/10.1007/s11214-020-00732-4

Housen, K. R., Schmidt, R. M., & Holsapple, K. A. (1983). Crater ejecta scaling laws: Fundamental forms based on dimensional analysis. *Journal of Geophysical Research*, *88*(B3), 2485–2499. https://doi.org/10.1029/JB088iB03p02485

Ivanov, M. A., Hiesinger, H., van der Bogert, C. H., Orgel, C., Pasckert, J. H., & Head, J. W. (2018). Geologic history of the northern portion of the South Pole-Aitken basin on the Moon. *Journal of Geophysical Research: Planets*, *123*(10), 2585–2612. https://doi.org/10.1029/2018JE005590

Jaumann, R., Hiesinger, H., Anand, M., Crawford, I. A., Wagner, R., Sohl, F., et al. (2012). Geology, geochemistry, and geophysics of the Moon: Status of current understanding. *Planetary and Space Science*, *74*(1), 15–41. https://doi.org/10.1016/j.pss.2012.08.019

Jozwiak, L. M., Head, J. W., & Wilson, L. (2018). Explosive volcanism on Mercury: Analysis of vent and deposit morphology and modes of eruption. *Icarus*, *302*, 191–212. https://doi.org/10.1016/j.icarus.2017.11.011

Kerber, L., Head, J. W., Blewett, D. T., Solomon, S. C., Wilson, L., Murchie, S. L., et al. (2011). The global distribution of pyroclastic deposits on Mercury: The view from MESSENGER flybys 1–3. *Planetary and Space Science*, *59*(15), 1895–1909. https://doi.org/10.1016/j.pss.2011.03.020

Kinczyk, M. J., Byrne, P. K., Prockter, L. M., Denevi, B. W., Buczkowski, D. L., Ostrach, L. R., & Miller, E. B. (2020). Progress on constructing the global geological map of Mercury. In *Planetary Geologic Mappers Meeting, abstract #7021*. Retrieved from https://www.hou.usra.edu/meetings/pgm2020/pdf/7021.pdf

Kumar, A. S. K., Roy Chowdhury, A. R., Banerjee, A., Dave, A. B., Sharma, B. N., Shah, K. J., et al. (2009). Hyper Spectral Imager for lunar mineral mapping in visible and near infrared band. *Current Science*, *96*(4), 496–499. Retrieved from https://www.jstor.org/stable/24105458

Klima, R. L., Denevi, B. W., Ernst, C. M., Murchie, S. L., & Peplowski, P. N. (2018). Global distribution and spectral properties of low-reflectance material on Mercury. *Geophysical Research Letters*, *45*(7), 2945–2953. https://doi.org/10.1002/2018GL077544

Langevin, Y. (1997). The regolith of Mercury: Present knowledge and implications for the Mercury Orbiter mission. *Planetary and Space Science*, *45*(1), 31–37. https://doi.org/10.1016/s0032-0633(96)00098-0

Leight, C., & Ostrach, L. R. (2018). Characterizing impact melt on Mercury. In *49th Lunar and Planetary Science Conference, abstract #2553*. Retrieved from https://www.hou.usra.edu/meetings/lpsc2018/pdf/2553.pdf

Lennox, A., Rothery, D. A., Wright, J., Balme, M. R., & Conway, S. J. (2021). Geological mapping of Mercury's south polar quadrangle (H-15). In *Europlanet Science Congress 2021, EPSC2021-737*. https://doi.org/10.5194/epsc2021-737

Leon-Dasi, M., Besse, S., & Doressoundiram, A. (2023). Deep learning investigation of Mercury's explosive volcanism. *Remote Sensing*, *15*(18), 4560. https://doi.org/10.3390/rs15184560

Lewang, A. M., Hiesinger, H., Bernhardt, H., Galluzzi, V., Guzzetta, L. G., & Massironi, M. (2018). Preliminary geologic map of the Beethoven basin, Mercury. In *49th Lunar and Planetary Science Conference, abstract #1846*. Retrieved from https://www.hou.usra.edu/meetings/lpsc2018/pdf/1846.pdf

Lucchetti, A., Pajola, M., Galluzzi, V., Giacomini, L., Carli, C., Cremonese, G., et al. (2018). Mercury hollows as remnants of original bedrock materials and devolatilization processes: A spectral clustering and geomorphological analysis. *Journal of Geophysical Research: Planets*, *123*(9), 2365–2379. https://doi.org/10.1029/2018JE005722

Lucey, P. G., & Riner, M. A. (2011). The optical effects of small iron particles that darken but do not redden: Evidence of intense space weathering on Mercury. *Icarus*, *212*(2), 451–462. https://doi.org/10.1016/j.icarus.2011.01.022

Malliband, C. C., Rothery, D. A., Balme, M. R., Conway, S. J., Pegg, D. L., & Wright, J. (2022). Geology of the derain quadrangle (H10), Mercury. *Journal of Maps*, *19*(1), 2112774. https://doi.org/10.1080/17445647.2022.2112774

Man, B., Rothery, D. A., Balme, M. R., Conway, S. J., Wright, J., Pegg, D. L., et al. (2023). Geology of the Neruda quadrangle (H13), Mercury. *Journal of Maps*, *19*(1), 2256353. https://doi.org/10.1080/17445647.2023.2256353

Mancinelli, P., Minelli, F., Pauselli, C., & Federico, C. (2016). Geology of the Raditladi quadrangle, Mercury (H04). *Journal of Maps*, *12*(sup1), 190–202. https://doi.org/10.1080/17445647.2016.1191384

Marchi, S., Chapman, C. R., Fassett, C. I., Head, J. W., Bottke, W. F., & Strom, R. G. (2013). Global resurfacing of Mercury 4.0–4.1 billion years ago by heavy bombardment and volcanism. *Nature*, *499*(7456), 59–61. https://doi.org/10.1038/nature12280

Marchi, S. S., Massironi, M., Cremonese, G., Martellato, E., Giacomini, L., & Prockter, L. M. (2011). The effects of the target material properties and layering on the crater chronology: The case of Raditladi and Rachmaninoff basins on Mercury. *Planetary and Space Science*, *59*(15), 1968–1980. https://doi.org/10.1016/j.pss.2011.06.007

Massironi, M., Rossi, A. P., Wright, J., Zambon, F., Poehler, C., Giacomini, L., et al. (2021). From morpho-stratigraphic to geo-stratigraphic units: The PLANMAP contribution. In *EGU General Assembly 2021, EGU21-15675*. https://doi.org/10.5194/egusphere-egu21-15675

McClintock, W. E., & Lankton, M. R. (2007). The Mercury Atmospheric and Surface Composition Spectrometer for the MESSENGER mission. *Space Science Reviews*, *131*(1–4), 481–521. https://doi.org/10.1007/s11214-007-9264-5

Murchie, S. L., Arvidson, R., Bedini, P., Beisser, K., Bibring, J. P., Bishop, J., et al. (2007). Compact Rconnaissance imaging spectrometer for Mars (CRISM) on Mars reconnaissance orbiter (MRO). *Journal of Geophysical Research*, *112*(E5), E05S03. https://doi.org/10.1029/2006JE002682

Murchie, S. L., Klima, R. L., Denevi, B. W., Ernst, C. M., Keller, M. R., Domingue, D. L., et al. (2015). Orbital multispectral mapping of Mercury with the MESSENGER Mercury Dual Imaging System: Evidence for the origins of plains units and low-reflectance material. *Icarus*, *254*, 287–305. https://doi.org/10.1016/j.icarus.2015.03.027

Namur, O., & Charlier, B. (2017). Silicate mineralogy at the surface of Mercury. *Nature Geoscience*, *10*(1), 9–13. https://doi.org/10.1038/NGEO2860

Neish, C. D., Blewett, D. T., Harmon, J. K., Coman, E. I., Cahill, J. T. S., & Ernst, C. M. (2013). A comparison of rayed craters on the Moon and Mercury. *Journal of Geophysical Research: Planets*, *118*(10), 2247–2261. https://doi.org/10.1002/jgre.20166

Nittler, L. R., Boujibar, A., Crapster-Pregont, E., Frank, E. A., McCoy, T. J., McCubbin, F. M., et al. (2023). Chromium on Mercury: New results from the MESSENGER X-ray Spectrometer and implications for the innermost planet's geochemical evolution. *Journal of Geophysical Research: Planets*, *128*(7), e2022JE007691. https://doi.org/10.1029/2022je007691

Nittler, L. R., Frank, E. A., Weider, S. Z., Crapster-Pregont, E. J., Vorburger, A., Starr, R. D., & Solomon, S. C. (2020). Global major-element maps of Mercury from four years of MESSENGER X-Ray Spectrometer observations. *Icarus*, *345*(July 2020), 113716. https://doi.org/10.1016/j.icarus.2020.113716

Nittler, L. R., Starr, R. D., Weider, S. Z., McCoy, T. J., Boynton, W. V., Ebel, D. S., et al. (2011). The major-element composition of Mercury's surface from MESSENGER X-ray spectrometry. *Science*, *333*(6051), 1847–1850. https://doi.org/10.1126/science.1211567

Orgel, C., Fassett, C. I., Michael, G., Riedel, C., van der Bogert, C. H., & Hiesinger, H. (2020). Re-examination of the population, stratigraphy, and sequence of Mercurian basins: Implications for Mercury's early impact history and comparison with the Moon. *Journal of Geophysical Research: Planets*, *125*(8), e2019JE006212. https://doi.org/10.1029/2019JE006212

Ostrach, L. R., Mest, S. C., Prockter, L. M., Petro, N. E., & Byrne, P. K. (2020). Finalizing the geologic map of the Borealis quadrangle (H-1) on Mercury. In *51st Lunar and Planetary Science Conference, absract #1211*. Retrieved from https://www.hou.usra.edu/meetings/lpsc2020/pdf/1211.pdf

Ostrach, L. R., Robinson, M. S., Whitten, J. L., Fassett, C. I., Strom, R. G., Head, J. W., & Solomon, S. C. (2015). Extent, age, and resurfacing history of the northern smooth plains on Mercury from MESSENGER observations. *Icarus*, *250*, 602–622. https://doi.org/10.1016/j.icarus.2014.11.010

Pegg, D. L., Rothery, D. A., Balme, M. R., & Conway, S. J. (2021). Explosive vents on Mercury: Commonplace multiple eruptions and their implications. *Icarus*, *365*, 114510. https://doi.org/10.1016/j.icarus.2021.114510

Pegg, D. L., Rothery, D. A., Balme, M. R., Conway, S. J., Malliband, C. C., & Man, B. (2021). Geology of the Debussy quadrangle (H14), Mercury. *Journal of Maps*, *17*(2), 718–729. https://doi.org/10.1080/17445647.2021.1996478

Pegg, D. L., Rothery, D. A., Conway, S. J., & Balme, M. R. (2021). A fault surface exposed on Mercury. *Planetary and Space Science*, *201*(July 2021), 105223. https://doi.org/10.1016/j.pss.2021.105223

Peplowski, P. N., Lawrence, D. J., Feldman, W. C., Goldsten, J. O., Bazell, D., Evans, L. G., et al. (2015). Geochemical terranes of Mercury's northern hemisphere as revealed by MESSENGER neutron measurements. *Icarus*, *253*(June 2015), 346–363. https://doi.org/10.1016/j.icarus.2015.02.002

Peplowski, P. N., & Stockstill-Cahill, K. (2019). Analytical identification and characterization of the major geochemical terranes of Mercury's northern hemisphere. *Journal of Geophysical Research: Planets*, *124*(9), 2414–2429. https://doi.org/10.1029/2019JE005997

Pieters, C. M., & Noble, S. K. (2016). Space weathering on airless bodies. *Journal of Geophysical Research: Planets*, *121*(10), 1865–1884. https://doi.org/10.1002/2016JE005128

Pöhler, C. M., Wright, J., Zambon, F., van der Bogert, C. H., Carli, C., Altieri, F., & Hiesinger, H. (2022). Enhancing geomorphological maps using geo-spectral maps on the example of the lunar Apollo basin. In *53rd Lunar and Planetary Science Conference, abstract #2094*. Retrieved from https://www.hou.usra.edu/meetings/lpsc2022/pdf/2094.pdf

Prockter, L. M., Ernst, C. M., Denevi, B. W., Chapman, C. R., Head, J. W., Fassett, C. I., et al. (2010). Evidence for young volcanism on Mercury from the third MESSENGER Flyby. *Science*, *329*(5992), 668–671. https://doi.org/10.1126/science.1188186

Prüsse, F., Galluzzi, V., Hiesinger, H., & van der Bogert, C. H. (2020). Geologic map and stratigraphy of the eastern Michelangelo quadrangle (H12), Mercury. In *51st Lunar and Planetary Science Conference, abstract #1851*. Retrieved from https://www.hou.usra.edu/meetings/lpsc2020/pdf/1851.pdf

Riner, M. A., & Lucey, P. G. (2012). Spectral effects of space weathering on Mercury: The role of composition and environment. *Geophysical Research Letters*, *39*(12), L12201. https://doi.org/10.1029/2012GL052065

Rothery, D. A., Babbs, T. L., Harris, A. J. L., & Wooster, M. J. (1996). Colored lava flows on the Earth: A warning to Io volcanologists. *Journal of Geophysical Research*, *101*(E11), 26131–26136. https://doi.org/10.1029/96JE02864

Rothery, D. A., Barraud, O., Besse, S., Carli, C., Pegg, D. L., Wright, J., & Zambon, F. (2021). On the asymmetry of Nathair Facula, Mercury. *Icarus*, *355*(February 2021), 114180. https://doi.org/10.1016/j.icarus.2020.114180

Rothery, D. A., Mancinelli, P., Guzzetta, L. G., & Wright, J. (2017). Mercury's Caloris basin: Continuity between the interior and exterior plains. *Journal of Geophysical Research: Planets*, *122*(3), 560–576. https://doi.org/10.1002/2017JE005282

Rothery, D. A., Marinangeli, L., Anand, M., Carpenter, J., Christensen, U., Crawford, I. A., et al. (2010). Mercury's surface and composition to be studied by BepiColombo. *Planetary and Space Science*, *58*(1–2), 21–39. https://doi.org/10.1016/j.pss.2008.09.001

Rothery, D. A., Massironi, M., Alemanno, G., Barraud, O., Besse, S., Bott, N., et al. (2020). Rationale for BepiColombo studies of Mercury's surface and composition. *Space Science Reviews*, *216*(66), 66. https://doi.org/10.1007/s11214-020-00694-7

Semenzato, A., Massironi, M., Ferrari, S., Galluzzi, V., Rothery, D. A., Pegg, D. L., et al. (2020). An integrated geologic map of the Rembrandt basin, on Mercury, as a starting point for stratigraphic analysis. *Remote Sensing*, *12*(19), 3213. https://doi.org/10.3390/rs12193213

Snyder, J. P. (1987). *Map projections: A working manual* (Vol. 1395). US Government Printing Office. https://doi.org/10.3133/pp1395

Solomon, S. C., McNutt, R. L., Gold, R. E., & Domingue, D. L. (2007). MESSENGER mission overview. *Space Science Reviews*, *131*(1–4), 3–39. https://doi.org/10.1007/s11214-007-9247-6

Solomon, S. C., Nittler, L. R., & Anderson, B. J. (Eds.) (2018). *Mercury: The view after MESSENGER*. Cambridge University Press. https://doi.org/10.1017/9781316650684

Stark, A., Preusker, F., Oberst, J., Matz, K.-D., Gwinner, K., & Roatsch, T. (2017). High-resolution topography from MESSENGER orbital stereo imaging—The H5 quadrangle "Hokusai". In *48th Lunar and Planetary Science Conference, abstract #2287*. Retrieved from https://www.hou.usra.edu/meetings/lpsc2017/pdf/2287.pdf

Thiessen, F., Besse, S., Staid, M. I., & Hiesinger, H. (2014). Mapping lunar mare basalt units in Mare Imbrium as observed with the Moon Mineralogy Mapper (M3). *Planetary and Space Science*, *104*(Part B), 244–252. https://doi.org/10.1016/j.pss.2014.10.003

Thomas, R. J., Rothery, D. A., Conway, S. J., & Anand, M. (2014). Hollows on Mercury: Materials and mechanisms involved in their formation. *Icarus*, *229*(Feruary 2014), 221–235. https://doi.org/10.1016/j.icarus.2013.11.018

Trask, N. J., & Guest, J. E. (1975). Preliminary geologic terrain map of Mercury. *Journal of Geophysical Research*, *80*(17), 2461–2477. https://doi.org/10.1029/JB080i017p02461

Vander Kaaden, K. E., & McCubbin, F. M. (2015). Exotic crust formation on Mercury: Consequences of a shallow, FeO-poor mantle. *Journal of Geophysical Research: Planets*, *120*(2), 195–209. https://doi.org/10.1002/2014JE004733

Vander Kaaden, K. E., McCubbin, F. M., Nittler, L. R., Peplowski, P. N., Weider, S. Z., Frank, E. A., & McCoy, T. J. (2017). Geochemistry, mineralogy, and petrology of boninitic and komatiitic rocks on the mercurian surface: Insights into the mercurian mantle. *Icarus*, *285*(15 March 2017), 155–168. https://doi.org/10.1016/j.icarus.2016.11.041

Weider, S. Z., Nittler, L. R., Starr, R. D., Crapster-Pregont, E. J., Peplowski, P. N., Denevi, B. W., et al. (2015). Evidence for geochemical terranes on Mercury: Global mapping of major elements with MESSENGER's X-Ray Spectrometer. *Earth and Planetary Science Letters*, *416*(15 April 2015), 109–120. https://doi.org/10.1016/j.epsl.2015.01.023

Whitten, J. L., Head, J. W., Denevi, B. W., & Solomon, S. C. (2014). Intercrater plains on Mercury: Insights into unit definition, characterization, and origin from MESSENGER datasets. *Icarus*, *241*, 97–113. https://doi.org/10.1016/j.icarus.2014.06.013

Wright, J., Byrne, P. K., & Rothery, D. A. (2021). Planet Mercury: Volcanism in a theatre of global contraction, with examples from the Hokusai quadrangle. *Journal of Volcanology and Geothermal Research*, *417*(September 2021), 107300. https://doi.org/10.1016/j.jvolgeores.2021.107300

Wright, J., Rothery, D. A., Balme, M. R., & Conway, S. J. (2019). Geology of the Hokusai quadrangle (H05), Mercury. *Journal of Maps*, *15*(2), 509–520. https://doi.org/10.1080/17445647.2019.1625821

Wright, J., Rothery, D. A., Balme, M. R., & Conway, S. J. (2021). PLANMAP—Deliverable D2.2 Mercury H-05 Hokusai quadrangle 5 crater classes (version 1) [Dataset]. Zenodo. https://doi.org/10.5281/zenodo.4773443

Wright, J., Zambon, F., Carli, C., Altieri, F., Pöhler, C. M., Rothery, D. A., et al. (2021). Geostratigraphic map of Rachmaninoff crater and Nathair Facula in the Hokusai Quadrangle (H05) of Mercury [Dataset]. Zenodo. https://doi.org/10.5281/zenodo.4773573

Yan, F., Li, N., & Hirota, K. (2021). QHSL: A quantum hue, saturation, and lightness color model. *Information Sciences*, *577*, 196–213. https://doi.org/10.1016/j.ins.2021.06.077

Yingst, R. A., Mest, S. C., Brent Garry, W., Williams, D. A., Berman, D. C., & Gregg, T. K. P. (2023). A geologic map of Vesta produced using a hybrid method for incorporating spectroscopic and morphologic data. *The Planetary Science Journal*, *4*(9), 157. https://doi.org/10.3847/psj/acebe9

Zambon, F., Carli, C., & Altieri, F. (2021). PLANMAP—Deliverable D4.4—Mercury/H05-Hokusai quadrangle spectral units map (Final) [Dataset]. Zenodo. https://doi.org/10.5281/zenodo.4772274

Zambon, F., Carli, C., Altieri, F., Combe, J.-P., van der Bogert, C. H., Pöhler, C. M., et al. (2021). Spectral analysis of Apollo Basins on the Moon through spectral units identification. In *EGU General Assembly 2021, EGU21-15831*. https://doi.org/10.5194/egusphere-egu21-15831

Zambon, F., Carli, C., Wright, J., Rothery, D. A., Altieri, F., Massironi, M., et al. (2022). Spectral units analysis of quadrangle H05-Hokusai on Mercury. *Journal of Geophysical Research: Planets*, *127*(3), e2021JE006918. https://doi.org/10.1029/2021je006918